공학박사 학위논문

Dynamics of Magnetic Vortices in Soft Ferromagnetic Nanodisks driven by Spin-polarized Currents: Micromagnetic Numerical and Analytical Calculations

강자성체 박막에서 스핀 편향 전류에 의한
스핀-소용돌이의 동적 거동에 관한 연구

2013 년 2 월

서울대학교 대학원

공과대학 재료공학부

최윤석

Dynamics of Magnetic Vortices in Soft Ferromagnetic Nanodisks driven by Spin-polarized Currents: Micromagnetic Numerical and Analytical Calculations

A THESIS
SUBMITTED TO THE FACULTY OF SEOUL
NATIONAL UNIVERSITY
BY

Youn-Seok Choi

Supervised by

Prof. Sang-Koog Kim

IN PRTIAL FULFILLMENT OF THE
REQUIRMENTS FOR THE DEGREE OF DOCTOR
OF PHILOSOPHY

February 2013

Department of Materials Science and Engineering
Graduate School
Seoul National University

Abstract

Dynamics of Magnetic Vortices in Soft Ferromagnetic Nanodisks
driven by Spin-polarized Currents:
Micromagnetic Numerical and Analytical Calculations

Youn-Seok Choi
Department of Materials Science and Engineering
Seoul National University

This thesis deals with dynamics of magnetic vortices in soft ferromagnetic nanodisk driven by spin-polarized currents with micromagnetic simulations and analytical calculations. For the numerical calculations, the Landau-Lifshitz-Gilbert equation is solved by the Object Oriented Micromagnetic Framework (OOMMF) and the LLG Micromagnetics Simulator. For the analytical calculations, Thiele's equation of motion in a single vortex model is used.

We observed sizable eigenfrequency shifts in spin-polarized dc-current-driven vortex gyrotropic motions in a soft magnetic nanodot, and clarified the underlying physics through micromagnetic numerical calculations. It was found that the vortex eigenfrequency is changed to higher (lower) values with increasing Oersted field strength associated with the out-of-plane dc current for the vortex chirality parallel (antiparallel) to the rotation sense of the Oersted field circumferential in-plane orientation. We studied magnetic vortex oscillations associated with vortex gyrotropic

motion driven by spin-polarized out-of-plane dc current by analytical and micromagnetic numerical calculations. Reliable controls of the tunable eigenfrequency and orbital amplitude of persistent vortex oscillations were demonstrated. This work provides an advanced step toward the practical application of vortex oscillations to persistent vortex oscillators in a wide frequency range of 10–2000 MHz and with high q factor.

Finally, we reported on an observation of transitions of the fourfold degenerate state of a magnetic vortex in soft magnetic nanodots by micromagnetic numerical calculations. The quaternary vortex states in patterned magnetic dots were found to be controllable by changing the density of out-of-plane dc or pulse currents applied to the dots. Each vortex state can be switched to any of the other states by applying different sequence combinations of individual single-step pulse currents. Each step pulse has a characteristic threshold current density and direction. This work offers a promising way for manipulating both the polarization and chirality of magnetic vortices.

Contents

iii

iv

List of Tables

List of Figures

Chapter 1

Introduction

Magnetic vortices are typically observed in patterned or continuous soft magnetic thin films. The magnetic vortex structure consists of in-plane curling and out-of-plane magnetizations at the core region [1-4]. This vortex state can be used as a memory unit cell in future memory devices, because not only does the magnetic vortex have two discrete states of up- and down-core orientations and two rotation senses (clockwise or counter-clockwise) of the in-plane magnetizations, but also the vortex state is stable in sufficiently small lateral sizes (> 20 nm) and thicknesses (> 2 nm) of nanoelements [5]. Also of recent and growing interest are the dynamic properties of a vortex in response to driving forces such as magnetic fields and spin-polarized currents, owing to its non-trivial static [1-6] and dynamic properties [7-10] as well as promising potential applications to information storage devices [11].

In particular, recent studies [12-15] have established that the spin-transfer torque of spin-polarized electric currents is a promisingly reliable means of switching the orientation of magnetizations in magnetic particles of submicron size or less. The spin-transfer torque thereby has been practically used in information storage [12] (e.g. MRAM) devices, due also

to its various advantages including low-power, ultrafast, and reliable information recording, and in frequency-tunable microwave oscillators [15, 16]. Moreover, the spin-transfer torque effect on magnetic vortex excitations in nanodot and nanopillar systems has begun to receive a great deal of attention owing to its potential applications to future information storage and microwave oscillator devices [10, 11, 17-26]. For instance, the current-driven vortex gyrotropic oscillation [17-21] and vortex core magnetization switching [10, 11, 22-26] in confined magnetic systems have been observed both experimentally[17-19, 21, 22] and numerically [10, 11, 20, 23-26].

In this thesis, the dynamics of magnetic vortex structure under various types of in-plane oscillating currents or out-of-plane dc currents were investigated using both analytical calculation and micromagnetic numerical simulations. First, we present on the observation of sizable shifts in the intrinsic eigenfrequency of vortex gyrotropic motions in a laterally confined thin-film nanodot by spin-polarized out-of-plane dc current. Second, we present on quantitative interpretations of vortex oscillations in a free standing soft magnetic nanodot driven by spin-polarized out-of-plane dc current, studied by analytical calculations and numerical simulations. Finally, we present the results of micromagnetic numerical simulations of out-of-plane-current-controlled switching between the fourfold degenerate vortex states.

This thesis is organized as follows. In Chapter 1, the magnetic vortex structure and the spin transfer torque are introduced. In Chapter 2, we provide the theoretical background to vortex gyrotropic motion by spin transfer torque effect. In Chapters 3 to 6, vortex dynamics driven by various types of current are presented with analytical calculations and micromagnetic numerical simulation results. Chapter 7 is a summary of this study.

1.1 Introduction to magnetic vortex structure

In submicron-sized ferromagnetic elements, the geometrical confinement in nanomagnets alters their energetics from the competition among several magnetic energies: the exchange energy resulting from the wave function of indistinguishable particles being subject to exchange symmetry, the magnetostatic energy due to the classical dipole-dipole interaction between magnetic moments, the magneto-crystalline anisotropy energy from the spin-orbit interaction, and additional energies induced by external forces, such as Zeeman energy.

In the absence of any external forces in a soft magnetic nanoelement, Zeeman energy and magnetocrystalline anisotropy energy are negligible. Therefore, the spin configurations are dominantly determined by the competition between the exchange energy and magnetostatic energy. The exchange energy favors electrons with parallel spins. The magnetostatic energy favors closed spin structure to prevent magnetic free poles from generating a stray magnetic field. As a result, magnetizations in the soft magnetic nanoelement are formed with an in-plane curling magnetization along the circular boundary, as shown in Fig. 1.1. The exchange energy will be immeasurable at the disk center because the variation of magnetization will be infinite. To avoid this singularity, a few-nm-scale magnetization

structure at the disk center has out-of-plane magnetization as shown in Fig. 1.2. This out-of-plane magnetization structure is called the 'vortex core'. Figure 1.3 shows direct measurement results of various vortex structures in nano-films. This vortex core plays a meaningful role in the dynamic motion of the magnetic vortex structure.

As mentioned above, the magnetic vortex structure is characterized by an in-plane curling magnetization of either counter-clockwise ($c = +1$) or clockwise ($c = -1$) orientation (denoted by chirality c) along with an out-of-plane core magnetization of either upward ($p = +1$) or downward ($p = -1$) orientation (represented by polarization p). Combinations of chirality and polarization of a vortex represent the fourfold degenerate state as shown in Fig. 1.4. This has been regarded as a promising candidate for future high-density, nonvolatile memory devices.
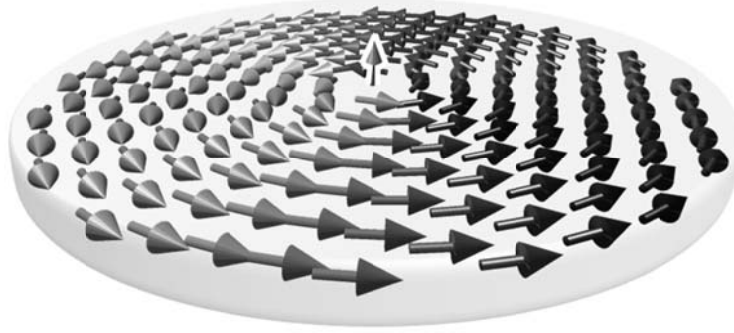
Fig. 1.1. Schematic illustration of the magnetic vortex structure. The magnetizations in a soft magnetic nanoelement are aligned along its circular boundary, forming an in-plane curling magnetization structure around the disk center to prevent magnetic free poles
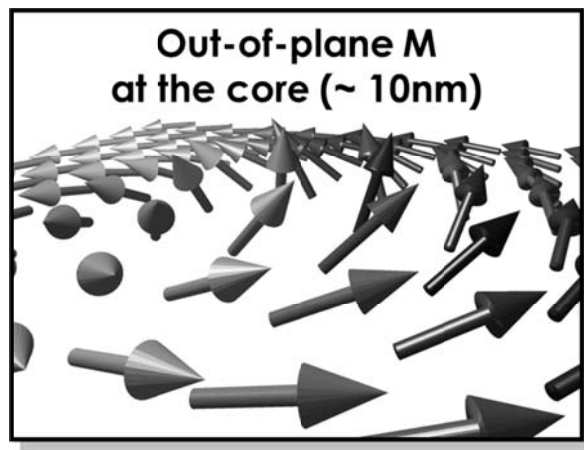
Fig. 1.2. Schematic illustration of the magnetic vortex core. A few-nm-scale out-of-plane magnetization structure at the center of the curling in-plane magnetization structure was developed.

6
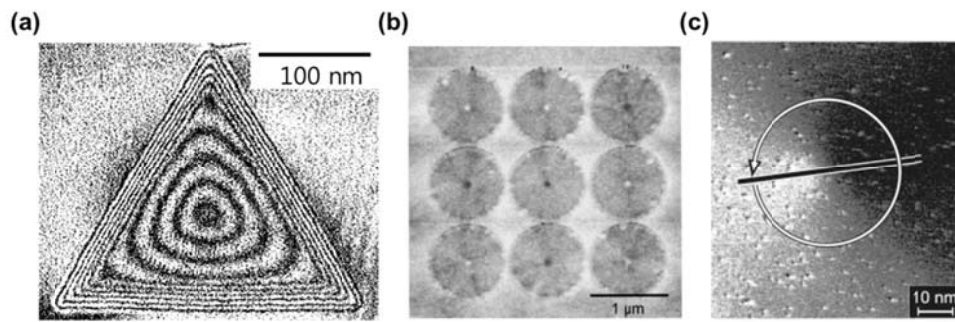
Fig. 1.3 direct measurements of a magnetic vortex structure. (a) Contour fringes which overlap individual particle micrographs [27]. (b) Vortex core structure using MFM [2]. (c) Experimental observation of internal spin structures of the vortex core in an iron nanoelement by spin-polarized scanning tunneling microscopy (SP-STM) [3].
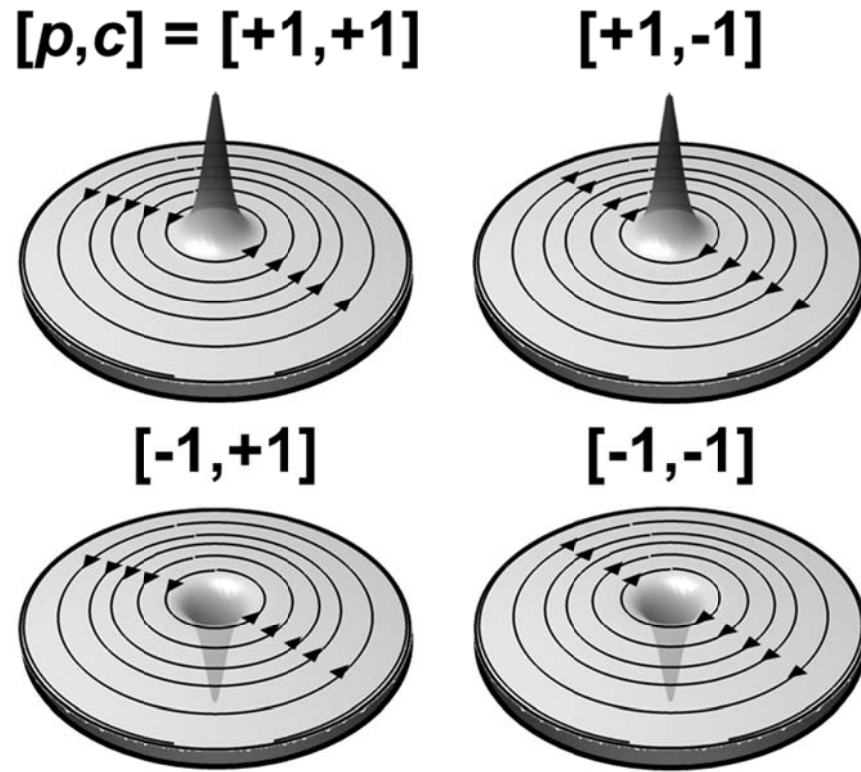
Fig. 1.4. Energetically equivalent four different states of a magnetic vortex according to the vortex core polarization p, and the chirality c. The height and color indicate the local out-of-plane magnetization components.

1.2 Introduction to spin transfer torque

Initial breakthroughs in the field of spintronics were related to the ability to read the state of a device, commonly the relative orientation of ferromagnetic layers in a spin valve or a magnetic tunnel junction [28, 29]. However, writing process is still in general accomplished by using magnetic fields. This has several disadvantages. First, magnetic fields lead to writing errors in closely-packed arrays of devices due to its difficulty of localizing spatiality. Second, spin switching with magnetic fields does not scale well because the switching field increases with the decreasing device sizes. Finally, static magnetic fields cannot be used to produce oscillations.

An efficient alternative to manipulating small ferromagnets with field was proposed in two influential papers in 1996 by Slonczewski [12] and Berger [13]. Their idea was that a spin-polarized current could be used to apply a torque to a ferromagnet. This would require much less current to produce a measurable reorientation of the ferromagnet than a magnetic field generated by Ampere's law, and would also be highly localized. The dynamics excited by this spin-transfer torque (STT) could be classified in two broad types: i) switching of the magnetization of a spin-valve between two stable configurations with great implications for the development of efficient, nonvolatile magnetic random access memory and ii) steady-state

9

oscillations of the magnetization under excitation by a direct current with great implications for the development of tunable oscillators. The first clear experimental observations of STT were made at Cornell [15, 30, 31]).

A more detailed understanding of the physics of STT can be obtained by looking at the quantum mechanical processes. A simple 1-dimensional model can be quite useful to illustrate the torque exerted by one electron incident on a ferromagnet [32]. We consider an incident spinor plane-wave wave function for a single electron with spin at angle θ to the z-axis:

$$\left| \psi_{incident} \right\rangle = Ce^{ikx} \left(\cos\frac{\theta}{2} \left| \uparrow \right\rangle + \sin\frac{\theta}{2} \left| \downarrow \right\rangle \right)$$

(1.2.1)

where *C* is a normalization factor. The potential step at the interfaces can be set to be 0 for spin-up electrons because of the exchange splitting the energy of the spin-up electrons in the ferromagnet is lower by a potential step of height than that of spin-down electrons. As a result, only spin-down electrons are reflected by the potential step of height. This is a good approximation for many commonly-used normal/ferromagnet interfaces, such as, Cu/Co or Cu/Ni. Then the transmitted and reflected wave functions can be calculated to be

$$\left| \psi_{transmitted} \right\rangle = C \left(e^{ikx} \cos\frac{\theta}{2} \left| \uparrow \right\rangle + e^{ikx} \frac{2k}{k+k_{\downarrow}} \sin\frac{\theta}{2} \left| \downarrow \right\rangle \right)$$

(1.2.2)

10

$$\left|\psi_{reflected}\right\rangle = Ce^{-ikx}\frac{k+k_{\downarrow}}{k+k_{\downarrow}}\sin\frac{\theta}{2}\left|\downarrow\right\rangle$$

(1.2.3)

where $k_{\uparrow} = k$ and $k_{\downarrow} = \sqrt{2m(E-\Delta)}/\hbar$, with a potential step of height Δ, the energy of the incident electron E (E > Δ), and the free electron mass m. The spin-transfer torque per electron is given by equation (1.2.4), which expresses the conservation of angular momentum

$$\mathbf{N} = -\int\hat{\mathbf{n}}\cdot\mathbf{Q}d^2\mathbf{R}$$

(1.2.4)

where $\mathbf{Q}$ is the spin current density per unit area of the ferromagnet, $\hat{\mathbf{n}}$ is the unit vector normal to the ferromagnet surface and the integral is over the surfaces of the ferromagnet. Thus, in order to calculate the amount of spin angular momentum transferred from the conduction electrons to the ferromagnet, it is necessary to compute the spin current densities per unit area of ferromagnet $\mathbf{Q}$ (incident, transmitted and reflected parts). At the normal/ferromagnet interface these can be computed from equation (1.2.5) by using the corresponding wave function given by equations (1.2.1), (1.2.2) and (1.2.3):

$$\mathbf{Q} = \frac{\hbar^2}{2m}\text{Im}(\psi^*\sigma\otimes\nabla\psi)$$

(1.2.5)

where σ is the Pauli matrices vector. By performing this calculation it is found that the transverse (in the x-y plane) component of the spin current density is entirely transmitted through the normal/ferromagnet interface,

11

while the reflected spin current has moment pointing along -z (antiparallel to the magnetization). Moreover, the transverse components of the spin current transmitted into the ferromagnet have sinusoidal terms with arguments of the form $(k_\uparrow - k_\downarrow)x$. This implies that the spin will precess in the ferromagnet with period $2\pi(k_\uparrow - k_\downarrow)$ (since spin-up and spin-down have different energies due to the exchange splitting). This leads to rapid classical dephasing of the transverse spin component, typically over a length scale of a few atomic spacings in a 3d ferromagnet. Consequently, the entire transverse component of the spin current is absorbed by the ferromagnet, and the spin current transmitted out of the ferromagnet is polarized with moment parallel to the magnetization. The total absorption of the transverse component leads to an expression for the torque per electron of the form

$$\mathbf{N} = AC\frac{\hbar^2}{2m}\sin(\theta)\hat{\mathbf{x}}$$

(1.2.6)

where A is the area of the ferromagnet (in a cross-section perpendicular to $\hat{x}$). Equation (1.2.9) is a good approximation for all-metallic systems. A number of differences exist between the physics of spin-torque in all-metallic systems and in magnetic tunnel junctions. In particular, in MTJ's there exists an additional contribution to the torque, along the y direction, which in metallic systems is negligibly small. Since the devices studied for this dissertation are all-metallic, I will not discuss the specifics of MTJ's

12

here. However, comprehensive reviews of STT in MTJ's can be found in Refs. [32] and [33].

The torque given by equation (1.2.6) is only a starting point to understanding the effects of STT in a real device. Since electrons in a normal metal are spin-unpolarized, the incident spin current is zero and so the torque would in general entirely vanish in a device consisting of a single normal/ferromagnet bilayer. Thus, all practical multilayer devices use the spin valve geometry, consisting of a ferromagnet/normal/ferromagnet trilayer. As mentioned earlier, in this case, it is necessary to consider the effect of multiple scattering events at the normal/ferromagnet interfaces. It is also important to consider whether transport through the normal spacer is ballistic or diffusive, and whether the structure is symmetric or not (some of the resulting expressions can be found in Refs. [34] and references therein). The basic form of the rate of change of the magnetization (for an asymmetric trilayer with ballistic transport across the normal spacer) is

$$\left(\frac{\partial \mathbf{M}_1}{\partial t}\right)_{STT} = -g_1(\theta)\frac{\gamma_0 \hbar I}{eV_1}\hat{\mathbf{M}}_1 \times \left(\hat{\mathbf{M}}_1 \times \hat{\mathbf{M}}_2\right)$$

(1.2.7)

where V_i is the volume of ferromagnetic layer i, e is the elementary charge, I is the applied current, γ_0 is the gyromagnetic ratio, $\hat{\mathbf{M}}_i$ are unit vectors for the magnetization of the two ferromagnetic layers, and $g_i(\theta)$ is an expression that depends on the details of the structure. It has the form [34]

13

$$g_i(\theta) = \frac{q_{+,i}}{A + B\cos\theta} + \frac{q_{-,i}}{A - B\cos\theta}$$

<div align="right">(1.2.8)</div>

with parameters A, B, $q_{+,i}$, $q_{-,i}$ that can be computed given the details of the structure, or can be obtained by fitting to experiment (although this is not easy for largely asymmetric structures).

Chapter 2

Research Background

2.1. Micromagnetics

In any realistic theory of magnetization processes, all three energy terms: exchange, anisotropy, and magnetostatic, must be taken into account. Moreover, Hemiltonian cannot be solved quantum mechanically unless rough approximations are introduced. Therefore, until a better theory is developed, the only way to solve the magnetization processes is to neglect quantum mechanics and to use classical physics in a continuous medium. Such a classical theory has been developed in parallel with the quantum-mechanical studies which simply ignore magnetostatics. Brown gave this theory the name micromagnetics.

Micromagnetics describes the magnetic behavior of ferromagnetic systems by a continuous vector field of classical magnetization vectors [35]. Magnetization vectors are spatial averages of discrete elementary magnetic moments of electron spins. The micromagnetic model is used to describe ferromagnetism semiclassically on length scales of some ten nanometers to some hundred microns, which would be too complex to be calculated quantum mechanically. It can correctly model the static structure of

ferromagnets, the formation of magnetic domains and domain walls, but also the dynamics of magnetic structures. The interaction between the magnetization vectors is modeled by effective fields, which have their origin in internal forces like the exchange coupling or the demagnetization coupling and external fields like the Zeeman field.

2.1.1. Landau-Lifshitz-Gilbert (LLG) equation

If the direction between a magnetic moment and an external field H is non-collinear, a torque on the magnetic moment is exerted as $d\mathbf{S}/dt = -\gamma^{-1}d\mathbf{m}/dt$. This leads to a gyration of the magnetic moment according to the equation,

$$\frac{d\mathbf{m}}{dt} = -\gamma\mathbf{m}\times\mathbf{H}.$$
(2.1.1)

L. D. Landau and E. M. Lifshitz [35] describes the motion of the magnetization in an effective field H_{eff}. [Fig. 2.1 (a)]

$$\frac{d\mathbf{M}}{dt} = -\gamma\mathbf{M}\times\mathbf{H}_{eff}$$
(2.1.2)

Gilbert introduced a phenomenological damping which encounters the gyration for example due to crystal impurities. In the Gilbert form of the Landau-Lifshitz equation, the damping term leads to a motion of the

16

magnetization, perpendicular to the velocity of the magnetization due to the gyration. [Fig. 2.1 (b)]

$$\frac{d\mathbf{M}}{dt} = -\gamma \mathbf{M} \times \mathbf{H}_{eff} + \frac{\alpha}{M_s} \mathbf{M} \times \frac{d\mathbf{M}}{dt}$$

(2.1.3)

In equation (2.1.3), the Gilbert damping parameter α determines the strength of the damping. At equilibrium both terms vanish to get a vanishing torque, which is the case for a collinear alignment of magnetization and effective field.

17
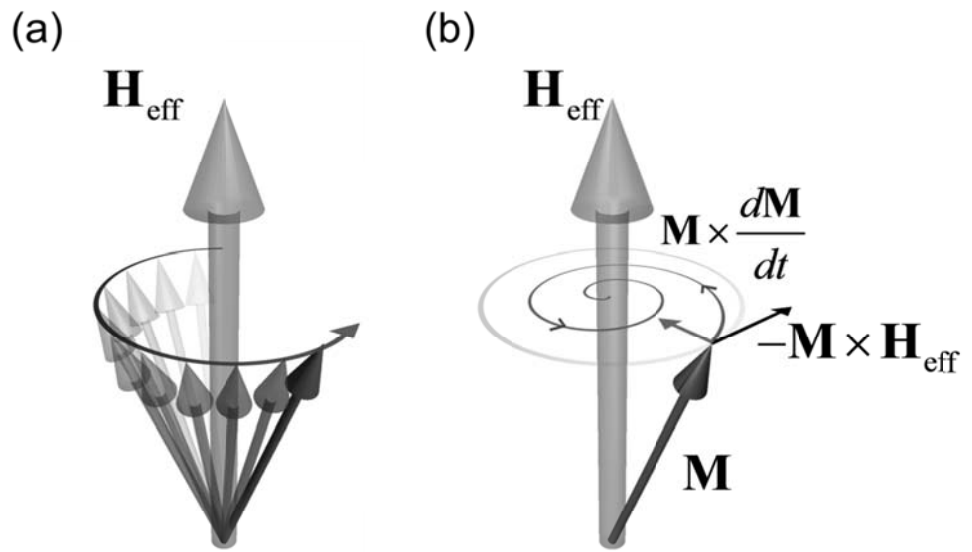
Fig 2.1 (From Ref. [36]) Schematic illustration of magnetization precession motion around the effective field without damping (a) and with damping (b).

2.1.2 Effective fields in the LLG equation

In the Landau-Lifshitz-Gilbert equation, the effective field $H_{\text{eff}} = H_{\text{ex}} + H_{\text{anisotropy}} + H_{\text{d}} + H_{\text{Zeeman}}$ is a sum of internal effective fields like the exchange H_{ex}, the anisotropy field $H_{\text{anisotropy}}$, and the demagnetization field H_{d} as well as external fields like the Zeeman field H_{Zeeman}. However, the anisotropy field, which describes the coupling between the magnetization vectors due to lattice symmetries [1], is not considered here because it is generally small in soft magnetic materials.

The exchange energy between two magnetization vectors can be derived by starting from the Heisenberg Hamiltonian of two spins S_i and S_j.

$$H = -J\mathbf{S}_i \cdot \mathbf{S}_j = -J\left|\mathbf{S}_i\right|\left|\mathbf{S}_j\right|\cos\phi \qquad (2.1.4)$$

When the cosine is expanded into a Taylor series assuming only small angles between the spins and the zero of the total energy is shifted by the constant term $-J|S_i||S_j|$, the exchange energy density reads

$$\hat{H} = \frac{J}{a^3}\mathbf{S}_i \cdot \mathbf{S}_j\left(\frac{\phi^2}{2}\right) \approx \frac{J}{2M_s^2 \cdot a}(\nabla\mathbf{M})^2 = \frac{A}{M_s^2}(\nabla\mathbf{M})^2 \qquad (2.1.5)$$

, where a is the lattice constant, ϕ is the angle between the spins, M_s is the saturation magnetization, and $A = J/2a$ is the exchange constant. The exchange energy of a ferromagnetic system can be obtained from a volume integration of equation (2.1.5) as follows.

19

$$E_{ex} = \frac{A}{M_s^2} \int (\nabla \mathbf{M})^2 \, dV$$

<div align="right">(2.1.6)</div>

And, the exchange field can be calculated from the variational derivative of the exchange energy [1].

$$H_{ex} = \frac{2A}{\mu_0 M_s^2} \nabla^2 \mathbf{M}$$

<div align="right">(2.1.7)</div>

The demagnetization field in a ferromagnetic body is derived by the Maxwell equations $\nabla \times \mathbf{H}_d = 0$ and $\nabla \cdot \mathbf{B}_d = 0$. The change of magnetic scalar potential at inside and outside magnetic bodies are $\Delta U_{in} = \nabla \cdot \mathbf{M}$ and $\Delta U_{out} = 0$, respectively. Boundary conditions on the surface to obtain U, H are $U_{in} = U_{out}$ and $\partial U_{in} / \partial n - \partial U_{out} / \partial n = \mathbf{M} \cdot \mathrm{n}$. As the results, the demagnetization field and energy can be derived as follows:

$$\mathbf{H}_d = -\int \mathbf{N}(\mathbf{r} - \mathbf{r}') \mathbf{M}(\mathbf{r}') dV'$$

<div align="right">(2.1.8)</div>

$$\mathbf{E}_d = -\frac{\mu_0}{2} \int \mathbf{H}_d \cdot \mathbf{M}(\mathbf{r}) dV$$

<div align="right">(2.1.9)</div>

with a demagnetization tensor $\mathbf{N}$.

Zeeman energy with the Zeeman field H_{Zeeman} reads

$$\mathbf{E}_{Zeeman} = -\mu_0 \int \mathbf{H}_{Zeeman} \cdot \mathbf{M} dV$$

<div align="right">(2.1.10)</div>

2.1.3 Spin transfer torque in the LLG equation

Spin-polarized electrons in a ferromagnetic system exert a torque on a non-uniform magnetization [13, 37]. This spin-torque driven by the spin-polarized electrons can be derived from the exchange interaction between an itinerant electron spin **s** and the localized electron spin **S**

$$\hat{H}_{sd} = \frac{|\mathbf{S}|J}{M_s} \mathbf{s} \cdot \mathbf{M}(\mathbf{r}, t) \tag{2.1.11}$$

with the exchange integral J. The itinerant spins **s** satisfy the continuity equation

$$\frac{d\mathbf{s}}{dt} + \nabla \cdot \hat{\mathbf{j}} = -\frac{1}{ih}\left(\left[s, \hat{H}_{sd}\right] + \left[s, \hat{H}_{scattering}\right]\right) \tag{2.1.12}$$

where $\hat{\mathbf{j}}$ is the spin-current operator, $\left[s, \hat{H}_{sd}\right]$ is the torque due to the exchange interaction, and $\left[s, \hat{H}_{scattering}\right]$ is the torque due to the spin relaxation as a consequence of scattering at impurities. Some conversions of equation (2.1.11) and equation (2.1.12) with approximations yield the extended Landau-Lifshitz-Gilbert equation [37]

$$\frac{d\mathbf{M}}{dt} = -\gamma \mathbf{M} \times \mathbf{H}_{eff} + \frac{\alpha}{M_s} \mathbf{M} \times \frac{d\mathbf{M}}{dt} - \frac{b_j}{M_s^2} \mathbf{M} \times \left(\mathbf{M} \times (\mathbf{j} \cdot \nabla)\mathbf{M}\right)$$
$$-\frac{\xi b_j}{M_s} \mathbf{M} \times (\mathbf{j} \cdot \nabla)\mathbf{M} \tag{2.1.13}$$

21

where b_j is the coupling constant between the itinerant spins and the magnetization, and j the electrical current density. The third term in equation (2.1.13) describes the adiabatic spin torque, where the electron spin is assumed to be parallel to the magnetization. The last term, called the non-adiabatic spin torque, includes deviations from the parallel alignment between electron spin and magnetization. In this thesis, the non-adiabatic spin torque is not considered because its effect is negligible in magnetic vortex dynamics, which is our main concern.

2.2. Analytical approach

In 1973, A. A. Thiele describes the steady-state motion of magnetic domains by collective coordinates rather than individual magnetization vectors, considering the gyrotropic force, the damping force, and the derivative of potential energy [38]. In the vortex-state soft magnetic nanodot, the vortex motion can be described by an effective Thiele's equation of motion for vortex collective coordinates with the assumption that magnetization distributions are independent along the dot thickness.

$$-\mathbf{G} \times \dot{\mathbf{X}} + \partial W / \partial \mathbf{X} - D\dot{\mathbf{X}} = 0 \qquad (2.2.1)$$

where $\mathbf{X} = (X, Y)$ is the VC position, $W(\mathbf{X})$ is the potential energy of the vortex core shifted from its equilibrium position ($\mathbf{X} = 0$), $\mathbf{G}$ is the gyrovector, and D is the damping tensor. The gyrovector $\mathbf{G}$ is given by $\mathbf{G} = p|G|$ with $G = -2\pi M_s L / \gamma$. The q is vorticity, it determines the direction of the in-plane magnetization components ($|q|$ is the vortex topological charge), the L is thickness of the vortex nanodot, and the γ is gyromagnetic ratio. The damping tensor D is given by $D = -\alpha\pi M_s L / \gamma (2 + \ln R / R_c)$ with some approximations. The α is damping constant, the R is radius of the vortex nanodot, the R_c is radius of the vortex core.

For small displacement **X**, the potential energy of the structure $W(\mathbf{X})$ can be expressed by a parabolic function of VC position, as

$$W(\mathbf{X}) = W_{exch}(\mathbf{X}) + W_{demag}(\mathbf{X}) = W_0 + \frac{1}{2}\kappa\mathbf{X}^2 \qquad (2.2.2)$$

where the exchange stiffness κ is the proportional coefficient of the restoring force to the vortex core displacement. Details about the exchange stiffness will be deeply discussed in the Chapter 4. The velocity of the vortex core $\dot{\mathbf{X}}$ can be expressed by the angular frequency vector and VC position as $\dot{\mathbf{X}} = \omega \times \mathbf{X}$. Inserting this representation form of the VC velocity $\dot{\mathbf{X}}$ into the equation (2.2.1), the equation (2.2.1) can be reformulated as

$$-|\mathbf{G}|\omega\mathbf{X} + \kappa\mathbf{X} - D\omega\mathbf{X} = 0. \qquad (2.2.3)$$

Through the equation (2.2.3), we can calculate the frequency of the VC gyrotropic motion, as

$$\omega = \frac{\kappa}{|\mathbf{G}| + D}. \qquad (2.2.4)$$

In the case of vortex dynamics driven by spin-polarized currents, spin-transfer torque force term is added into the equation (2.2.1), as

$$-\mathbf{G} \times \dot{\mathbf{X}} + \partial W / \partial\mathbf{X} - D\dot{\mathbf{X}} - \mathbf{F}_{STT} = 0. \qquad (2.2.5)$$

This additional term is changed by the applied method of spin-polarized currents. In the case of an in-plane oscillating current, the spin-transfer torque force term is presented as $\mathbf{F}_{STT} = \mathbf{G} \times \mathbf{v}_s$ with drift velocity

24

of the electron spin $\mathbf{v}_s = a^3 \mathbf{j}_s / 2eS$. The a is lattice constant, the $\mathbf{j}_s$ is current density, the e is electron charge, and the S is magnitude of spin. On the other hand, in the case of an out-of-plane dc current, the term is presented as $\mathbf{F}_{\text{STT}} = 2\pi S_{\text{pol}} a_{\text{T}} j_0 (\hat{\mathbf{z}} \times \mathbf{X})$ with the STT coefficient a_{T}. The modified analytical calculation using equation (2.2.5) will be treated in next sections.

Chapter 3

Vortex core switching driven by in-plane current

From a technological point of view, it is thus of great importance to readily control the VC orientation. However, such switching has been known to be possible only with the application of a strong static magnetic field. i.e, H > 2.5 kOe along the VC orientation in order to overcome a huge energy barrier to the VC reversal. On the contrary, recently Waeyenberge et al. [39] experimentally demonstrated, using a time-resolved scanning X-ray microscope, that a VC in a Permalloy (Ni80Fe20; Py) square dot can be switched even with a small-amplitude oscillating magnetic field. In addition, spin-polarized current has been used to manipulate the magnetic vortex state in nanodots [40, 41], and ac in-plane current was used to excite VC eigenmodes [19]. Moreover, electrical switching of VC orientation was promisingly demonstrated by both numerical calculation and experimental verification [22]. These achievements would be sufficient to attract much attention, because not only the non-volatile bi-states of a magnetic vortex with either up- or down-core orientation can be scaled down with its ultrahigh density, but also VC bi-states can be readily manipulated by currents passing directly through the vortex structure. However, detailed understanding of current-driven VC switching is still lacking.

In this section, we report numerical calculations of the magnetization dynamics of a magnetic vortex state in a Py nanodot in response to ac currents of different amplitude I_0 and frequency v around the resonant eigenfrequency v_0 of the dot. The non-trivial mechanism of VC reversal and its criteria related to the velocity of VC motion are elucidated.

3.1 Simulation conditions

We used the Landau-Lifshitz-Gilbert simulator [42], which enables the calculation of magnetization dynamics based on the LLG equation of motion with an additional term describing the torque exerted by spin-polarized current [12, 13, 37]. This term was used in the form of $\vec{T}_s = -(\vec{u} \cdot \nabla)\vec{m}$, where $\vec{u} = -\vec{j}Pg\mu_B / (2eM_s)$ with the current density j, the spin polarization P of the current ($P = 0.7$ for Py), the g-factor g, the electron charge e, and the Bohr magneton μ_B. $\vec{T}_s$ corresponds to the "adiabatic" approximation [37], which for the case of magnetic vortex dynamics was justified by Kasai et al. [19]. In the modeling, we chose a diameter of $2R = 600$ nm and a thickness of $L = 20$ nm for the Py nanodisk. This model yields an initial magnetization state of a single magnetic vortex with the down-core orientation and counter-clockwise in-plane magnetization rotation, as shown in Fig. 3.1(a).

The vortex gyrotropic eigenfrequency in the given model was determined to be $v_0 = 300$ MHz. In-plane ac currents, $I(t) = I_0 \sin(2\pi v t)$, of various v and I_0 values were applied along the x axis of the dot.
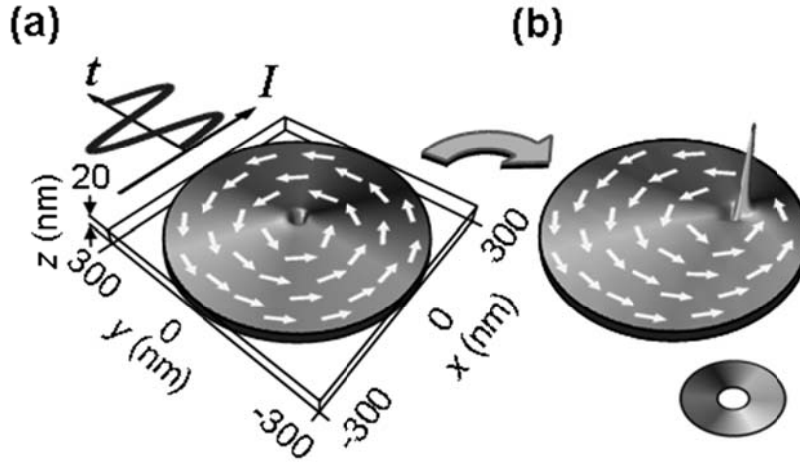
Fig. 3.1 The geometry and dimension of the model Py nanodot. The in-plane ac current is applied along the x axis to the dot. The initial vortex state of the downward core orientation located in the middle of the disk and with counter-clockwise in-plane magnetization orientation in (a) is switched to the upward core orientation with the same in-plane magnetization rotation in (b). The colors display the local magnetization, as indicated by the color wheel. The height in the images represents the out-of-plane component of the local magnetization s.

3.2 Vortex core reversal and critical velocity

Under the applied ac current, the VC position deviates from its initial center position and shows its spiral motion around the dot center, and then the VC orientation can be switched opposite to the initial core orientation under some conditions, as shown in Fig. 3.1(b).

Figure 3.2(a) shows the resultant dynamic evolution of the VC motion at (I_0, v) = (7.2 mA, 300 MHz), illustrated by perspective-view images of the out-of-plane magnetization components (represented by height and color) at the indicated times. The applied values of v and I_0 correspond to the v_0 and a current density $j_0 = 6 \times 10^7$ A/cm^2, respectively. Upon the application of $I(t)$, the vortex core begins to move and deviate in position from the dot center, and then shows its spiral-like motion in the time interval of $t = 0 - 16$ ns, shown in the top of Fig. 3.2(b). When the VC velocity reaches a critical value v_c = 340 ± 20 m/s in the given dot, the initial down-core orientation is switched to the up-core orientation (see moment ⑤). The reversed VC changes the sense of its gyrotropic motion from the clockwise to counter-clockwise rotation [7]. For $v = v_0$, it is clear that VC reversal repeatedly takes place when the reversed VC velocity reaches v_c = 340 ± 20 m/s again, as seen in Fig. 3.2(c). The first VC

30

reversal occurs in a time of 12.75 ns, and the next serial reversals occur every 3.3 ± 0.15 ns.
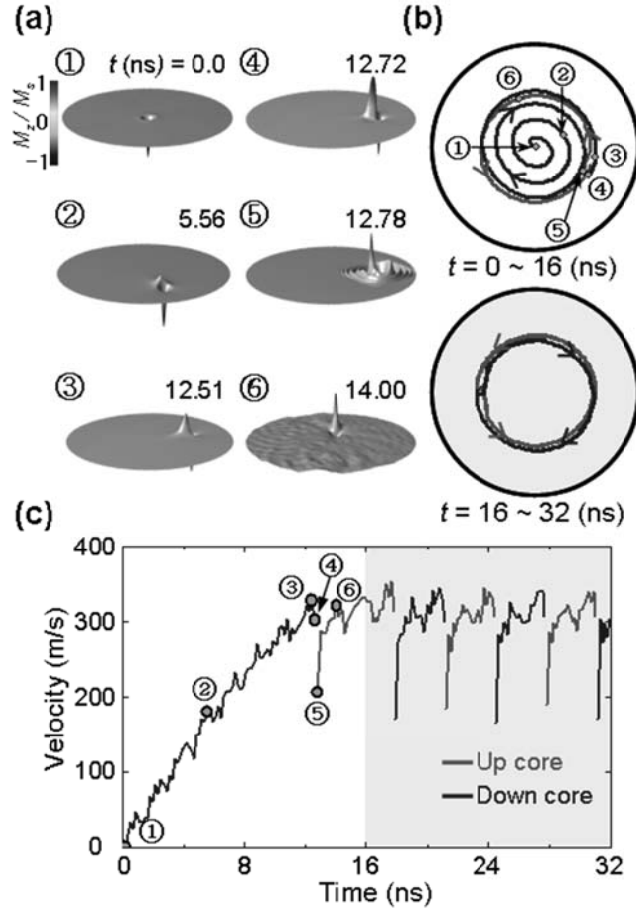
Fig. 3.2 (a) A series of snapshot images illustrating the dynamic evolution of the VC gyrotropic motion and its reversal process, and the resultant spin-wave emission, driven by an ac current of $I_0 = 7.2$ mA (current density $j_0 = 6 \times 10^7$ A/cm^2) and $v = 300$ MHz. (b) The orbit trajectories of the VC gyromotions. (c) The velocity of the VC moving along the trajectories as a function of time. The blue and red colors indicate the initial VC and the reversed VC, respectively. The numbers noted on the trajectory curve and velocity-vs-time curve, indicating each stage of the dynamic evolution, are the same as those shown in Fig. 3.2(a).

32

3.3 Effects of frequency and current density on vortex core reversal

In order to investigate the effects of v and j_0 on VC reversal, we conducted the same simulations with different j_0 and v values. The VC trajectories in the time period of $t = 0 - 16$ ns and the VC velocity-vs-time are shown for different v values at $j_0 = 6\times10^7$ A/cm^2 in Fig. 3.3, and for different j_0 values at $v = v_0 = 300$ MHz in Fig. 3.4. The results showed that the VC reversal can be effectively manipulated at v close to v_0, and even at $v = v_0$ a sufficiently large current density is required for the VC switching. For example, at $v = v_0$, current densities less than 4×10^7 A/cm^2 do not lead to VC reversal, but affecting the orbital size of the VC gyromotions. According to the velocity-vs-time curves shown in Fig. 3.3 and Fig. 3.4, VC reversal always occurs when the VC velocity reaches $\upsilon_c = 340 (\pm 20)$ m/s in the given dot. It is obvious that the VC orientation switches very effectively in the cases of $v \sim v_0$, and that at the given value of v, there exists a certain threshold value of j_0 for VC reversal. Driving force parameters such as v and j_0 do not affect the value of υ_c that is given for the material and geometry.
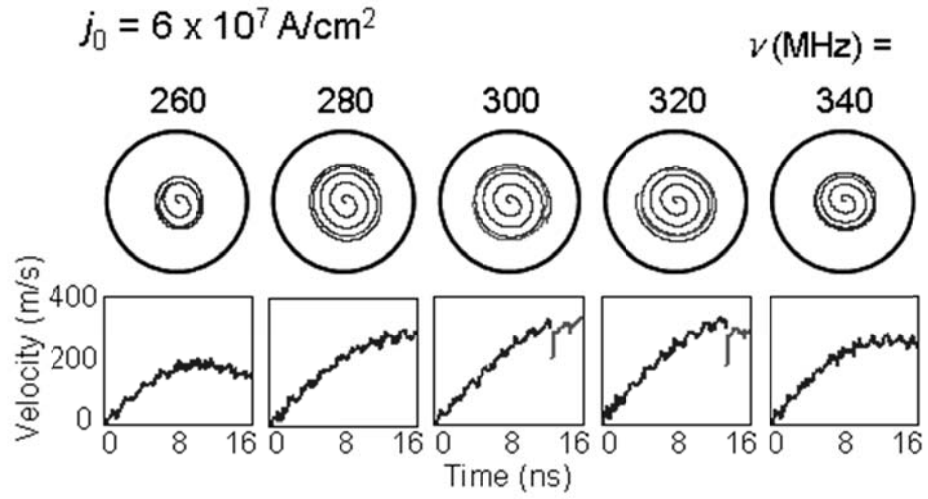
Fig 3.3 The VC trajectories before the VC reversal or both before and after, and the velocities of the VC gyromotions for the various current frequencies as indicated. For $j_0 = 6 \times 10^7$ A/cm^2, v varies from 260 to 340 MHz in increments of 20 MHz. The blue and red colors indicate the initial VC before its reversal and the reversed VC after, respectively.
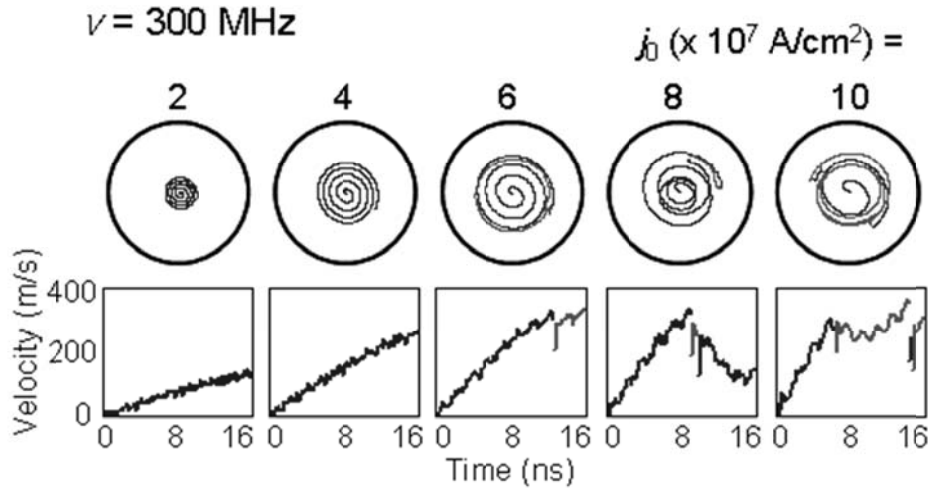
Fig 3.4 The VC trajectories before the VC reversal or both before and after, and the velocities of the VC gyromotions for the various current densities as indicated. For $v = v_0 = 300$ MHz, j_0 varies from 2×10^7 to 1×10^8 A/cm^2 in increments of 2×10^7 A/cm^2. The blue and red colors indicate the initial VC before its reversal and the reversed VC after, respectively.

3.4 Underlying mechanism of the vortex core reversal

As the next step, it is necessary to clarify the underlying mechanism of the observed VC switching. We plotted the detailed dynamic magnetization distributions in a local area nearby the initial VC position at the times indicated in Fig. 3.5. A close look at the microstructure of each stage of the dynamic evolution shows that the VC reversal process is more complicated than a simple switching between the down- and up-core orientations. With increasing VC velocity, the initial magnetic vortex structure begins to deform, the VC deformation maximizes, and the in-plane curling magnetization structure becomes more elongated (indicated in moment ແ). These deformations lead to the concentration of the dipolar and exchange energies, and hence their energy densities markedly increase in the area nearby the core position. The out-of-plane magnetization component in this area also increases at the expense of the dipolar energy as the in-plane magnetization structure of the magnetic vortex becomes more deformed. Thus, a vortex-antivortex (V-AV) pair ($V^{\uparrow}$ - $\overline{V}^{\uparrow}$) eventually nucleates nearby the initial VC (at moment ແ). The nucleated V-AV pair has parallel core-orientations opposite to that of the original VC ($V^{\downarrow}$). Due to their attractive interaction, accordingly, the nucleated $\overline{V}^{\uparrow}$ and the original $V^{\downarrow}$ move closer [43], and finally annihilate (see moment ແ),

36

reducing the exchange energy that was previously stored as a result of the presence of the additional VCs in the $V^{\uparrow}$-$\overline{V}^{\uparrow}$ pair. Therefore, the magnetic vortex state in the dot after the reversal process is the remaining $V^{\uparrow}$ (see moment ᔥ). These processes occur continuously and repeatedly in response to the AC current, as already shown in Fig. 3.2. Immediately after V-AV annihilation, the excess energy offered by the AC current is emitted in the form of spin waves (see moment ᔥ) [4]. The spin waves, of discrete GHz-range frequencies, are emitted from the V-AV annihilation point, then propagate to the dot border and reflect from it, forming an interference pattern [44]. We found that this unexpected dynamic process is mediated by the serial process of the creation of a V-AV pair and the subsequent annihilation of the initial magnetic vortex and the created AV. Such a reversal mechanism has also been found in VC reversals driven by small-amplitude in-plane oscillating magnetic fields [39, 43-45]. Current- and magnetic-field-driven VC reversals show their similarity in the underlying mechanism, and are pure dynamic ultrafast (< 0.1 ns) processes [see the time interval from state ᔥ to ⑤ in Fig. 3.2(c)], reflecting the relation of the time scale to the strong exchange interaction. This allows the VC reversal to occur on a-few-tens-of-ps scale with relatively low currents of 6-10 mA in the given dot when $v \sim v_0$.

The results in this section amount to a signal opportunity to use VCs for ultrafast information storage and recording in the sub-THz frequency range and as a source of high-amplitude spin waves.
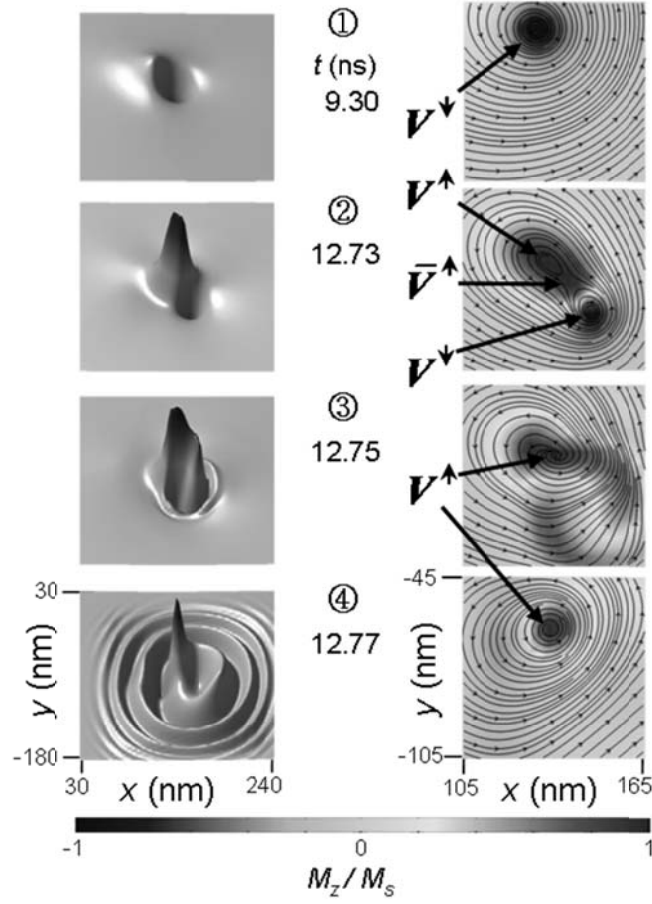
Fig. 3.5 Snapshot images of the local magnetization distribution taken at the indicated times from the perspective (left column) and plane (right column) views. The color and height of the surfaces in the left column indicate the local out-of-plane magnetization normalized by the saturation value, M_z/M_s. The streamlines with the small arrows in the right column indicate the in-plane direction of the local magnetization. The symbols $V^{\uparrow,\downarrow}$ and $\bar{V}^{\uparrow,\downarrow}$ represent V and AV, respectively. Their superscripts indicate the "up" ($\uparrow$) and "down" ($\downarrow$) core orientations.

39

Chapter 4

Vortex core oscillation driven by out-of-plane current: Oersted field effect

In this section, we report on the observation of sizable shifts in the intrinsic eigenfrequency of vortex gyrotropic motions in a laterally confined thin-film nanodot. The physical origin of this behavior was quantitatively understood by considering the Zeeman contribution of the spin-polarized-current-induced circumferential Oersted field (OH) to the effective potential energy of a displaced VC. We found an analytical equation that relates the eigenfrequency shift to the current density and its flowing direction. This results provides a reliable means of manipulating the intrinsic eigenfrequency, $\nu_D = \frac{1}{2\pi}\omega_D$, of a given vortex state using an external driving force of spin-polarized out-of-plane dc currents, which manipulation might be applicable to frequency-tunable oscillators in the sub-GHz range without additional application of external magnetic fields.

4.1 Simulation conditions

To conduct micromagnetic numerical calculations of vortex dynamics associated with a low-frequency translation mode (the so-called gyrotropic motion) in a nanodot, we used the LLG code [42], which utilizes the Landau-Lifshitz-Gilbert equation of motion, which includes the STT term [12, 13], expressed as $\mathbf{T}_{\mathrm{STT}} = (a_{\mathrm{STT}}/M_s)\mathbf{M}\times(\mathbf{M}\times\hat{\mathbf{m}}_P)$ with $a_{\mathrm{STT}} = \frac{1}{2\pi}h\gamma Pj_0/(\mu_0 2eM_s L)$. $\hat{\mathbf{m}}_P$ is the unit vector of the spin polarization orientation, h the Plank's constant, γ the gyromagnetic ratio, P the degree of spin polarization, j_0 the current density, μ_0 the vacuum permeability, e the electron charge, M_s the constant magnitude of magnetization, and L the thickness of a free magnetic layer. We employed, as a model, a circular-shaped Py nanodot of $2R = 300$ nm and $L = 20$ nm [see Fig. 4.1(a)]. An equilibrium vortex state in the given dot can be characterized by the vortex integers of the chirality c and the polarization p: $c = +1$ (-1) corresponds to the counter-clockwise (CCW) [clockwise (CW)] rotation sense of the in-plane curling magnetization, and $p = +1$ (-1) corresponds to the upward (downward) magnetization orientation of the VC. For example, the vortex state of $c = +1$ and $p = +1$ is illustrated in Fig. 4.1(a). The initial states of the vortex polarization and the direction of the polarizer are $p = +1$ and $\hat{\mathbf{m}}_P$ being in the -z direction (antiparallel to the vortex polarization), respectively.

Spin-polarized currents were applied with a duration time of 100 ns through the dot of the vortex state toward the $+z$ direction. Then, we investigated the vortex gyrotropic motions in the linear regime for 100 ns upon the application of the currents.
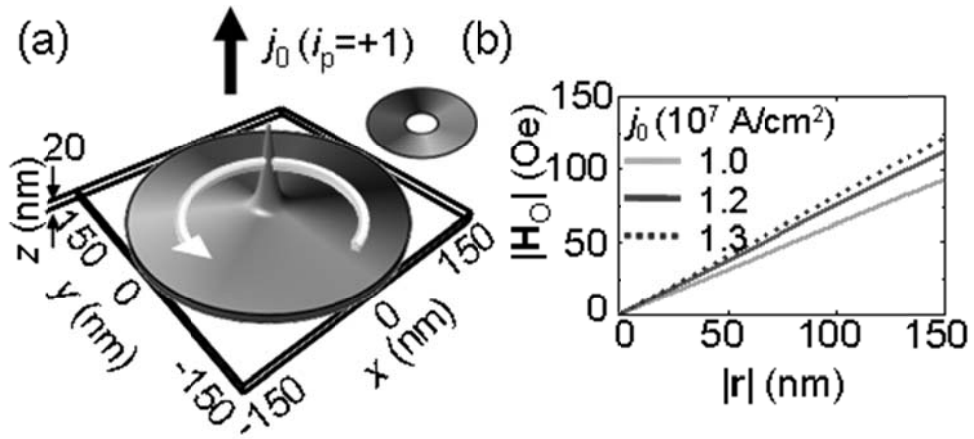
Fig. 4.1 (a) Vortex state with upward magnetization orientation of its VC and CCW in-plane curling magnetization in circular Py dot of indicated dimensions. The color and height display the local in-plane magnetization and out-of-plane magnetization components, respectively. (b) Oersted field strength profile along radial distance |**r**| for indicated different j_0 values.

4.2 Eigenfrequency shift by Oersted field effect

In order to examine how the OH effect of spin-polarized out-of-plane dc currents is considerable in vortex gyrotropic motions, first we calculated the strength profile of the OH produced for different j_0 values based on Biot-Savart's formulation $\mathbf{H}_O(\mathbf{r}) = \frac{1}{2} j_0 i_p (\hat{\mathbf{z}} \times \mathbf{r})$, where $\mathbf{r}$ is the radial vector from the center position ($\mathbf{r} = 0$) and i_p is the direction of the applied currents, i.e., $i_p = +1$ (-1) corresponding to the $+z$ ($-z$) direction. The CCW and CW rotation senses of the circumferential OH are thus determined simply by the sign of i_p, i.e., corresponding to $i_p = +1$ and -1, respectively. For $i_p = \pm 1$, the OH strength profile versus $|\mathbf{r}|$ for different j_0 values are shown in Fig. 4.1(b). At the center of the dot, $\left| \mathbf{H}_O(0) \right| = 0$ for all of the j_0 values, but sufficiently large values of $\sim$ 100 Oe are obtained at the edge, which values can modify vortex gyrotropic motions driven by spin-polarized currents, as will be described.

Figure 4.2 displays the orbital trajectories of the spiral motions of a VC in the linear regime driven by a spin-polarized current with $j_0 = 1.3 \times 10^7$ A/cm^2 for the three different indicated cases: case I), only the STT effect in the absence of the OH; cases II) and III), the STT effect considering the OH with its circumferential in-plane orientation parallel (P) and antiparallel (AP) to a given vortex chirality ($c = +1$ or -1), respectively.

These three different cases hereafter are abbreviated as cases I) 'STT only', II) 'STT+OH(P)', and III) 'STT+OH(AP)'. For all of the cases, the observed orbital trajectories show spirally rotating motions with exponentially increasing orbital radii. In cases of in-plane oscillating currents [10, 11, 19, 22, 24] or fields [11, 46], the increasing orbital radius converges exponentially to a certain steady-state orbital radius,[11, 24, 46] by contrast, the out-of-plane spin-polarized current-driven vortex gyrotropic motions show exponentially increasing orbital radii with distinctive rates for the different cases of I, II, and III. Such an exponentially increasing (or decreasing) orbital radius can be considered to be one of the characteristic dynamic properties of spin-polarized out-of-plane current-driven vortex gyrotropic motions.
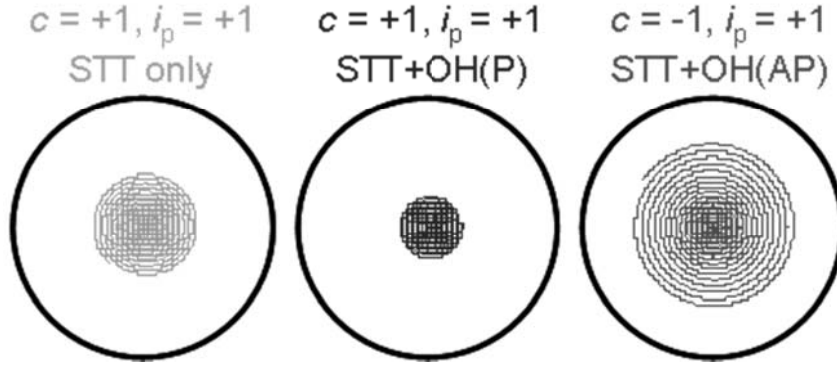
Fig. 4.2 Orbital trajectories of moving VC under spin-polarized out-of-plane dc current of $j_0 = 1.3 \times 10^7$ A/cm^2 for indicated different cases, as noted in text and above each figure. Here, the chirality c of the vortex state and the rotation sense of the OH are noted above each figure.

From Fast Fourier Transforms (FFTs) of the time variation of the *x*-component of the VC position, we obtained FFT spectra as a function of the frequency. As revealed in the inset of Fig. 4.3, the eigenfrequencies and their full width at half maximum (FWHM) in the cases of I, II, and III, are very contrasting. The value of $\frac{1}{2\pi}\omega_D$ = 580 MHz (FWHM: 30 MHz) in case I was shifted to a higher value, 645 MHz (FWHM: 50 MHz) in case II, and to a lower value, 515 MHz (FWHM: 40 MHz) in case III. In order to quantitatively clarify the observed OH effect on the eigenfrequency shifts, we plotted the modified eigenfrequency $\frac{1}{2\pi}\omega_D'$ as a function of j_0, for those j_0 values larger than a critical current density, j_{cri}. Here j_{cri} is defined as a threshold current density above which the vortex gyrotropic motions can be excited with a continuously increasing orbital radius. From the simulations, the critical current density for STT only is obtained to be j_{cri} = 6.4×10^6 A/cm^2 , and j_{cri} = 6.8×10^6 A/cm^2 for STT+OH(P) and 6.1×10^6 A/cm^2 for STT+OH(AP). These deviations for the cases of additional OH effect are within ± 5% of that for STT only. It is clearly shown that $\frac{1}{2\pi}\omega_D'$ increases (decreases) linearly with increasing OH strength for the parallel (antiparallel) orientation between c and the rotation sense of OH (Fig. 4.3). From the linear fits (lines) to the simulation results (symbols), we could find a relationship between $\frac{1}{2\pi}\omega_D'$ and j_0. Note that $d\omega_D'/dj_0$ is zero for STT only (case I), and that for cases II and III, the

47

values of $\frac{1}{2\pi}\omega_D'$ converge to $\frac{1}{2\pi}\omega_D$ = 580 MHz, with the approach to

$j_0 = 0$, according to the slope $\frac{1}{2\pi}d\omega_D'/dj_0 = \pm 5.0$ cm^2/A·s. The sign of

$\frac{1}{2\pi}d\omega_D'/dj_0$ is determined by the sign of the product of c and i_p, i.e., $ci_p =$

+1 (−1) corresponds to the parallel (antiparallel) orientation between the

vortex chirality and the rotation sense of OH.
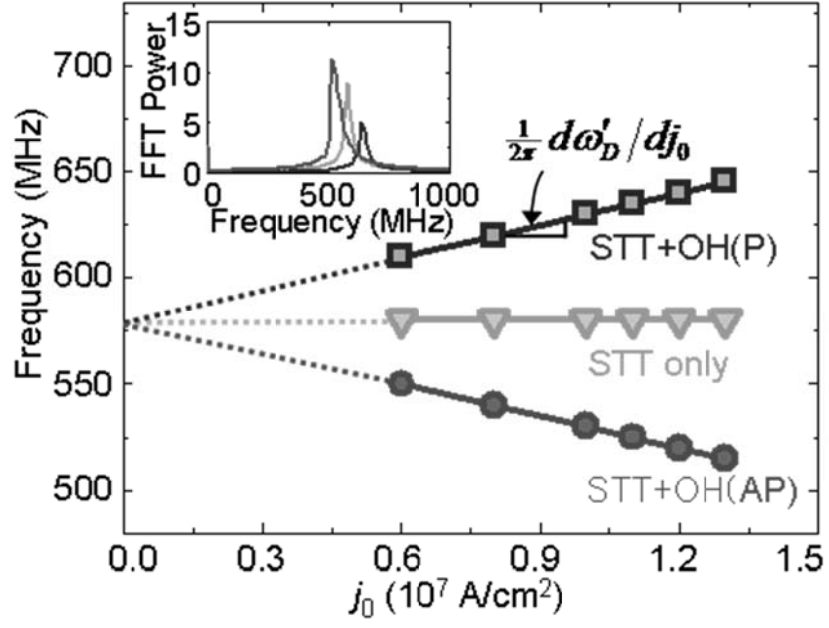
Fig. 4.3 Dominant frequency variations with j_0 for three different cases. The inset shows the FFT power versus frequency, calculated from the time-varying x-component of the VC position under a spin-polarized current with $j_0 = 1.3 \times 10^7$ A/cm^2.

4.3 The underlying physics of Oersted field effect

Next, in order to elucidate the underlying physics of the OH effect on the modification of the ω'_D value, and to obtain a quantitative relation between ω'_D and j_0, we used the known relation $\omega_D \simeq \omega_0 = \kappa_0 / |G|$ for a small Gilbert damping parameter, e.g., here $\alpha = 0.01$ [10, 11], where G is the gyrovector constant, and κ_0 is the intrinsic stiffness coefficient of the potential energy [7]. For a given dot, G and κ_0 are constant, being 6.14×10^{-10} erg·s/cm^2 and 2.3 erg/cm^2, respectively, for the model used in this study, and thus $\frac{1}{2\pi}\omega_0 = 596$ MHz, which value is close to that (580 MHz) obtained from the simulation result. Therefore, the modified ω'_D values can be evaluated directly from the modified κ values due to the OH contribution. For a small displaced VC, the potential energy is given as $W(\mathbf{X}) = W(0) + \kappa_0 \mathbf{X}^2 / 2$, considering both the exchange and magnetostatic energy. To obtain the relation of the OH contribution to κ, the κ values can be determined from the plots of $W_{tot}(\mathbf{X})$ versus $|\mathbf{X}|^2$ [see the left top of Fig. 4.4], where the $W_{tot}(\mathbf{X})$ were obtained from the simulation results for cases I, II, and III. As seen in the right top of Fig. 4.4, it is evident that the Zeeman energy term modifies the slope of the W_{tot} versus $|\mathbf{X}|^2$ curve in each case. In contrast, the magnetostatic and exchange energy contributions to

50

the modification of the $W_{tot}(\mathbf{X})$ versus $|\mathbf{X}|^2$ curves in cases I, II, and III are

negligible.
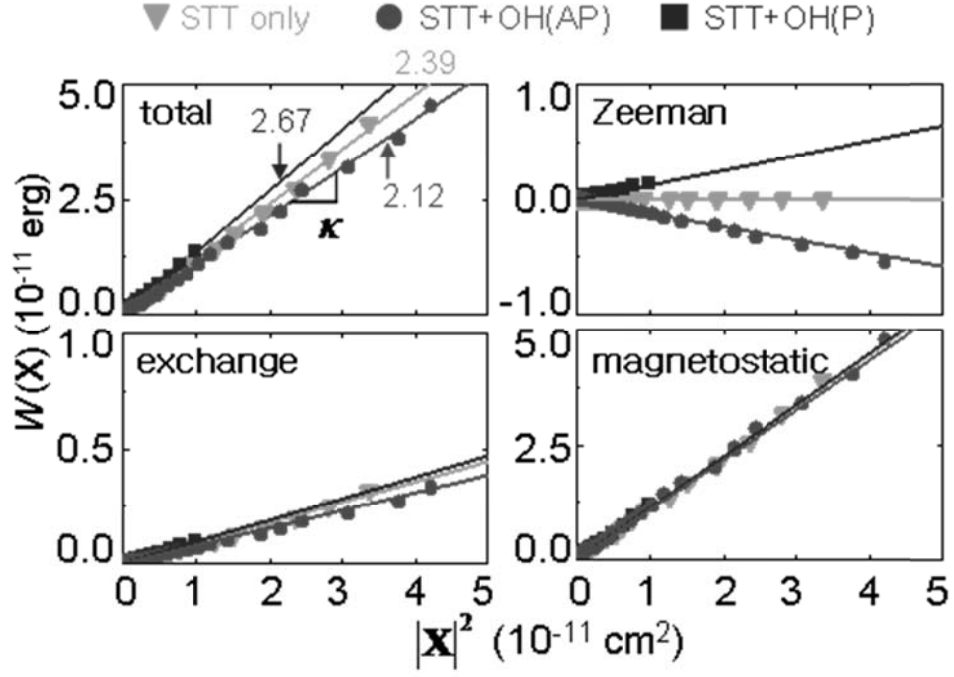
Fig. 4.4 W(X)-versus-$|X|^2$ curves for total, individual Zeeman, exchange, and magnetostatic contributions for $j_0 = 1.3 \times 10^7$ A/cm^2. Each colored line indicates a linear fit to the corresponding simulation result (symbol) for each case. The linear fit values in the left top are as follows: $\kappa = 2.39$, 2.67, and 2.12 erg/cm^2 for case I, II, and III, respectively.

52

The linear fits to the W_{tot} versus $|\mathbf{X}|^2$ curves for the different j_0 values allow us to numerically estimate the κ values according to j_0 for cases I, II, and III and which curves were plotted in Fig. 4.5. It is clear that κ for STT only (case I) is independent of j_0 (see Fig. 4.6) and thus it turns to be κ_0, and being numerically estimated to be 2.39 erg/cm^2. By contrast, in the two cases including the OH effect, the κ values vary linearly with j_0, thereby yielding the slope $d\kappa / dj_0 = \pm 1.9 \times 10^{-8}$ erg/A. Consequently, the effective potential energy accounting for the OH effect can be rewritten as $W_{tot}(\mathbf{X}) = W_{tot}(0) + [\kappa_0 + \kappa_{OH}]\mathbf{X}^2 / 2$ for the case considering the OH contribution, where κ_{OH} is an additional term associated with the OH contribution of out-of-plane currents. From the slopes of the κ versus j_0 curves shown in Fig. 4.5, we can relate $\kappa_{OH} = \pm \eta j_0$ with a proportional constant value of $\eta = 1.9 \times 10^{-8}$ erg/A for the given Py dot, leading to the relation of $\omega'_D \simeq [\kappa_0 + \kappa_{OH}]/|G| = [\kappa_0 \pm \eta j_0)]/|G|$. As a result, the eigenfrequency shift, $\Delta\omega_D = \omega'_D - \omega_D$ is given simply by $\Delta\omega_D \simeq \kappa_{OH}/|G| = \pm \eta j_0 /|G|$. The value of $\Delta\omega_D$ is positive (negative) for the positive (negative) value of ci_p. The rotation sense of the OH relative to the vortex chirality affects the stiffness coefficient of the potential energy for a vortex motion. It is given that for $ci_p = +1$, $\kappa_0 + \kappa_{OH} > \kappa_0$ and for $ci_p = -1$,

$\kappa_0 + \kappa_{OH} < \kappa_0$. From the estimated value of $\eta = |d\kappa/dj_0|$ = 1.9×10^{-8} erg/A and $G = 6.14 \times 10^{-10}$ erg·s/cm² for the model dot used here, we obtained the value of $\frac{1}{2\pi}\eta/|G| = 4.92$ cm²/A·s, which is in quite good agreement with the value of $\frac{1}{2\pi}|d\omega_D'/dj_0| = 5.0$ cm²/A·s obtained from the observed eigenfrequency shifts shown in Fig. 4.3. Finally, we can relate the eigenfrequency shifts with the OH effect, resulting in the analytical form of $\frac{1}{2\pi}\Delta\omega_D \simeq (ci_p\eta/|G|)j_0$. This result quantitatively verifies that the observed eigenfrequency shifts originate from the Zeeman contribution of the OH of spin-polarized currents to the potential energy stiffness coefficient, and vary with both the applied current density and its direction.
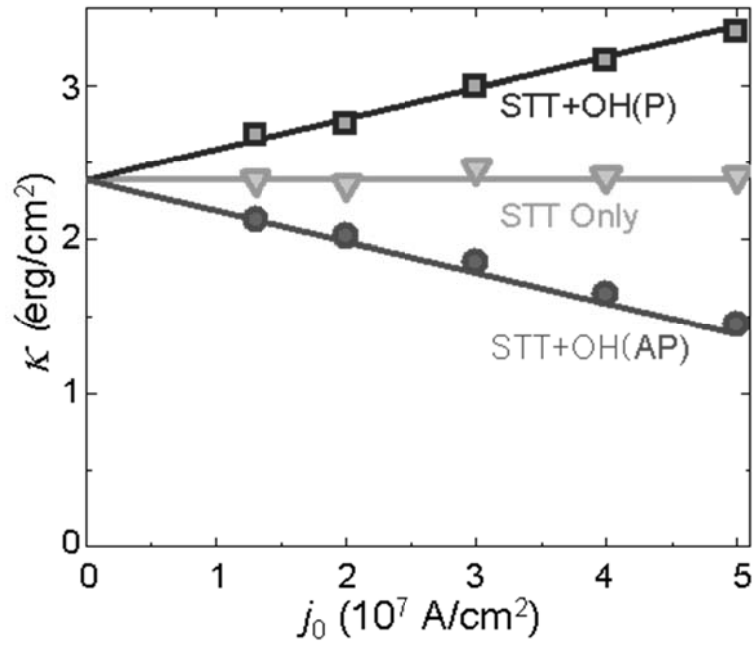
Fig. 4.5 κ versus j_0 relationships for all three cases.
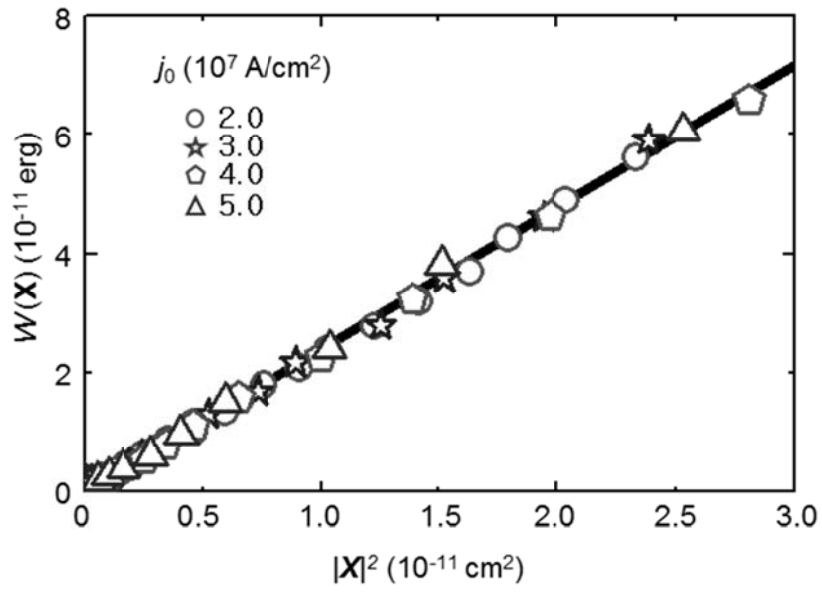
Fig. 4.6 The total potential energy as a function of $|\mathbf{X}|^2$ for case I with different j_0 values.

Chapter 5

Vortex core oscillation driven by out-of-plane current:

Analytical calculation and

micromagnetic numerical study

In this section, we report on quantitative interpretations of vortex oscillations in a free standing soft magnetic nanodot driven by spin-polarized out-of-plane dc current, studied by analytical calculations and numerical simulations. We consider both the STT effect of spin-polarized currents acting directly on vortex nonuniform magnetization structure and the comparable Oersted field effect accompanying the current flow. The results obtained from this section reveal a reliable means of manipulating the eigenfrequency and the orbital amplitude of VC translation motions in an oscillating manner in a dot of a different vortex state, by out-of-plane dc currents flowing through a perpendicular magnetization polarizer. The quantitative understanding of dc current driven vortex oscillations and its manipulation by key driving parameters, as found in this section, can offer an advanced step in its practical applications to persistent vortex oscillators with a tunable eigenfrequency (f) in its broad range of 10 to 2000 MHz and

a high $f/\Delta f$ value, without applying additional large in-plane and perpendicular magnetic fields.

5.1 Simulation conditions

To quantitatively understand and explore the underlying physics of vortex oscillations in nanodots driven by spin-polarized out-of-plane dc currents, we chose two complementary approaches: micromagnetic numerical and analytical calculations using a model system of the circular shaped Py nanodot of $2R = 300$ nm diameter and $L = 20$ nm thickness, as shown in Fig. 5.1. The ground states of energetically equivalent four different vortex structures can be characterized by two vortex integers, the chirality c and the polarization p. The term $c = +1$ (-1) corresponds to the counter-clockwise (CCW) [clockwise (CW)] rotation sense of the in-plane curling magnetization, and the term $p = +1$ (-1) corresponds to the upward (downward) magnetization orientation of the VC. Figure 1 shows a specific vortex state having $c = \pm 1$ and $p = +1$. In the present simulations, we used the LLG commercial code [42] that utilizes the Landau-Lifshitz-Gilbert equation of motion [35], including the STT term [12] expressed as $\mathbf{T}_{\mathrm{STT}} = (a_{\mathrm{STT}} / M_s)\mathbf{M} \times (\mathbf{M} \times \hat{\mathbf{m}}_P)$ with $a_{\mathrm{STT}} = \frac{1}{2\pi} h\gamma P j_0 / (\mu_0 2 e M_s L)$. The $\hat{\mathbf{m}}_P$ is the unit vector of spin polarization direction, h the Plank's constant, γ the gyromagnetic ratio, P the degree of spin polarization, j_0 the current density, μ_0 the vacuum permeability, e the electron charge, M_s the constant magnitude of magnetization. Out-of-plane dc currents were applied toward

59

the $+z$ direction for sufficiently long time, 100 ns in this study, through the polarizer with perpendicular magnetization pointing in either $+z$ or $-z$ direction. Non-ignorable OHs accompanying the out-of-plane dc currents were taken into account using Biot-Savart's formulation. Here, we define the directions of the applied current and the spin polarization as i_p and S_pol, respectively: the sign of $i_\mathrm{p} = +1$ (-1) and $S_\mathrm{pol} = +1$ (-1) corresponds to the $+z$ $(-z)$ direction. Thus, the rotation sense of the circumferential OH is determined simply by the sign of i_p, i.e., $i_\mathrm{p} = +1$ (-1) represents the CCW (CW) rotation sense of the OH in-plane orientation.
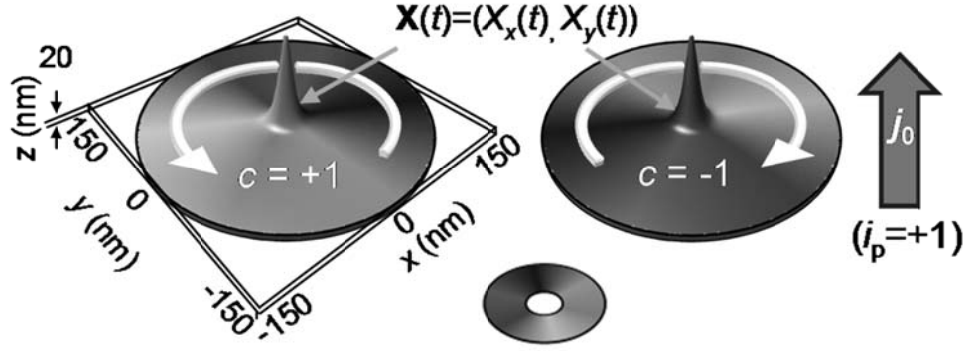
Fig. 5.1 Vortex state with p = +1 (upward magnetization orientation at the VC) and c = +1 (CCW in-plane curling magnetization) in a Py nanodot with the indicated thickness and diameter. The color and height indicate the in-plane orientation of local magnetizations and the out-of-plane magnetization components, respectively. The direction of current flow is indicated by the large arrow pointing in the +z direction.

5.2 Micromagnetic numerical simulation

Figure 5.2 shows examples of the characteristic features of the translational motions of a VC driven by specific values of $j_0 = 1.5, 0.1, 0.52$, and 0.48×10^7 A/cm^2, which were obtained from simulations with considering both the STT and the accompanying OH with its circumferential in-plane orientation parallel (P) to $c = +1$ and antiparallel (AP) to $c = -1$. By the definitions of c and i_p, the P (AP) configuration can also be denoted as $c \cdot i_\mathrm{p} = +1$ (-1). The first and middle rows in Fig. 5.2 represent the observed trajectories of the orbital motions and the y components, respectively, of the VC position vector, $\mathbf{X}(t) = [X_x(t), X_y(t)]$ in the dot (x-y) plane, where X_x and X_y are the x- and y- components of $\mathbf{X}(t)$. The initial VC position, $\mathbf{X}_0$, at $t = 0$ was displaced to $[-1.5$ nm, 25.5 nm$]$ for $c = +1$ or $[1.5$ nm, -25.5 nm$]$) for $c = -1$ by a static field of 100 Oe along the x-direction before applications of out-of-plane dc currents.

The simulation results reveal that spirally rotating motions of a VC with the exponentially increasing, decreasing, and almost constant orbital radii (shown in Figs. 5.2(a), 5.2(b), and 5.2(c), respectively), along with the corresponding eigenfrequencies (third row of Fig. 5.2) are remarkably contrasting for different j_0 values chosen here. The first thing to stress here is the observed blue- and red-shifts of the eigenfrequency from 580 MHz at

$j_0 = 0$ (i.e., without application of current) for $c \cdot i_\mathrm{p} = +1$ and -1, respectively. The second one is the remarkable variation of the orbital amplitude of VC motions with different j_0 values. For $j_0 = 1.5$ (0.1) $\times 10^7$ A/cm^2, the orbital amplitude exhibits its increase (decrease) with time from the corresponding $\mathbf{X}_0$. By contrast, for the application of $j_0 = 0.48$ (0.52) $\times 10^7$ A/cm^2 for the $c \cdot i_\mathrm{p} = -1$ (+1) configuration, the VC is allowed to be maintained around the initial orbit, being analogous to the resonant motion of a VC on a steady-state circular orbit that is driven by harmonic oscillating in-plane magnetic fields and currents [10, 11, 24, 47]. Also, the numerical estimates of the eigenfrequency, f, the full width at half maximum (FWHM: Δf), and $f/\Delta f$ values in frequency spectra are given in Table 5.1. Such remarkable variations of the eigenfrequency and the orbital amplitude with j_0 have not been understood quantitatively and analytically, whereas the quantitative understanding of these dynamic properties are crucial in the determination of key parameters to control vortex oscillations that are practically applicable to self-sustained nano-oscillators. Also, the phase of a moving VC position and the $f/\Delta f$ values are crucial factors to be understood from an application point of view.
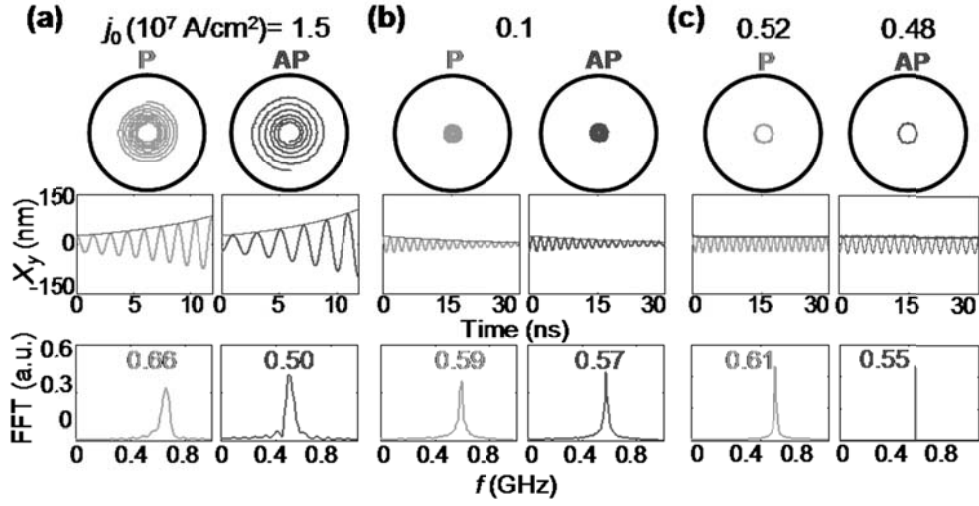
Fig. 5.2 VC translation motions driven by spin-polarized out-of-plane dc current of (a) $j_0 = 1.5 \times 10^7$ A/cm², (b) 0.1×10^7 A/cm², and (c) 0.48×10^7 and 0.52×10^7 A/cm² for indicated antiparallel (AP: $c \cdot i_p = -1$) and parallel (P: $c \cdot i_p = +1$) configurations, as noted in text. The orbital trajectories of a moving VC are shown in the top row as well as the time variations of the y components of the VC position in the middle row and their FFT power spectra in the bottom row. The FFT power spectra obtained from the VC motion during $t = 0 \sim 100$ ns.

j_0 (10^7 A/cm^2)	1.5		0.1		0.52	0.48
ci_p	+1	−1	+1	−1	+1	−1
f (MHz)	660±0.7	500±0.6	586±0.7	572±0.7	612±0.3	550±0.06
Δf (MHz)	60±1.4	60±1.3	38.7±1.5	33.4±1.5	14.9±0.5	6.5±0.04
$f/\Delta f$	11±2.7	8.3±0.2	15.1±0.7	17.1±0.9	41.1±1.4	84.6±0.5

TABLE 5.1. Estimates of the eigenfrequency (f), FWHM (Δf), and $f/\Delta f$ factor, obtained from Gaussian fits to the simulation results shown in Fig. 5.2. The FFT power spectra shown in Fig. 5.2 were obtained from time oscillations of the y component of a moving VC position for a time duration, $t = 0 \sim 100$ ns.

5.3 Analytical calculations

To elucidate the underlying physics of the observed dynamic behaviors and to search for key parameters for reliably controlling the eigenfrequency and the orbital amplitude of VC oscillations in a nanodot of a different size and of a different vortex state characterized by c and p, we analytically calculated $\mathbf{X}(t)$ in the dot (x-y) plane. In this analytical calculation, we used the linearized Thiele's equation [38] of motion by employing the force term, $\mathbf{F}_{\mathrm{STT}} = 2\pi S_{\mathrm{pol}} a_{\mathrm{T}} j_0 (\hat{\mathbf{z}} \times \mathbf{X})$ with the STT coefficient $a_{\mathrm{T}} = a_{\mathrm{STT}} L M_s / (\gamma j_0) = \frac{1}{2\pi} h P / (2\mu_0 e)$. Similar to the derivation of the gyroscopic force and drag (damping) force under an assumption of a steady-state motion of the $\mathbf{M}$ configuration as in Ref. [38], the force term $\mathbf{F}_{\mathrm{STT}}$ driven by spin-polarized currents of S_{pol} can be expressed as,

$$\mathbf{F}_{\mathrm{STT}} = \left[F_{\mathrm{STT},x}, F_{\mathrm{STT},y} \right] = -\left(a_{\mathrm{T}} / L \right) j_0 S_{\mathrm{pol}} \left[\int_V dV \left(\mathbf{m} \times \partial \mathbf{m} / \partial x \right) \cdot \hat{\mathbf{z}}, \int_V dV \left(\mathbf{m} \times \partial \mathbf{m} / \partial y \right) \cdot \hat{\mathbf{z}} \right]$$

where $\mathbf{m} = \mathbf{M} / M_s$. By integrating numerically or analytically the above equation, we can formulate the $\mathbf{F}_{\mathrm{STT}}$ term for a given $\mathbf{M}$ structure, i.e., for a vortex $\mathbf{M}$ structure with the "surface charge free" model, as $\mathbf{F}_{\mathrm{STT}} = \delta S_{\mathrm{pol}} a_{\mathrm{T}} j_0 (\hat{\mathbf{z}} \times \mathbf{X})$ with a proportional constant $\delta = 2\pi$. However, for the real vortex $\mathbf{M}$ structure obtained from micromagnetic simulations, we obtained a different value of $\delta = 5.31$, which is 25 % smaller than the value of $\delta = 2\pi$ for the analytical calculation mentioned above. This

66

discrepancy indicates that the real **M** configuration for the dynamic vortex motions driven by the STT term obtained from micromagnetic simulations differs from that of the "surface charge free" model.

The governing equation of VC translation (gyrotropic) motions in the linear regime is written in terms of a moving VC position vector $\mathbf{X}(t)$ as

$$-\mathbf{G} \times \dot{\mathbf{X}} + \partial W / \partial \mathbf{X} - D\dot{\mathbf{X}} - \mathbf{F}_{\mathrm{STT}} = 0 \,, \tag{5.3.1}$$

where $\mathbf{G} = -p|G|\hat{\mathbf{z}}$ is the gyrovector with its constant G, and $D < 0$ is the damping constant. The potential energy of a displaced VC in a circular dot can be expressed as $W(\mathbf{X}, t) = W(\mathbf{X} = 0) + \kappa \mathbf{X}^2(t)/2$ with the stiffness coefficient κ. Equation (5.3.1) is rewritten in the matrix form:

$$-\begin{bmatrix} D & p|G| \\ -p|G| & D \end{bmatrix} \dot{\mathbf{X}} + \begin{bmatrix} \kappa & 2\pi S_{\mathrm{pol}} a_{\mathrm{T}} j_0 \\ -2\pi S_{\mathrm{pol}} a_{\mathrm{T}} j_0 & \kappa \end{bmatrix} \mathbf{X} = 0 \,. \tag{5.3.2}$$

The general solution of equation (5.3.2) is simply given as $\mathbf{X}(t) = \mathbf{X}_0 \exp(-i\omega t)$ with the angular eigenfrequency ω. Inserting this solution into equation (5.3.2) leads to the analytical form of the eigenfrequency, $\omega = (\kappa + i2\pi S_{\mathrm{pol}} a_{\mathrm{T}} j_0) / (p|G| - iD)$, and the relation of the X_{x} and X_{y}, i.e., $X_y = iX_x$. Since $\omega = \omega_{\mathrm{R}} + i\omega_{\mathrm{I}}$ is a complex function, the real and imaginary terms can be expressed as

$$\omega_{\mathrm{R}} = \left(\kappa p|G| - 2\pi S_{\mathrm{pol}} a_{\mathrm{T}} j_0 D \right) / \left(G^2 + D^2 \right) \tag{5.3.3}$$

67

$$\omega_{\mathrm{I}} = \left(\kappa D + 2\pi S_{\mathrm{pol}} a_{\mathrm{T}} j_0 p |G| \right) / \left(G^2 + D^2 \right)$$ (5.3.4)

The VC position vector as a function of time in response to out-of-plane dc current is thus given by $\mathbf{X}(t) = \mathbf{X}_0 \exp(\omega_{\mathrm{I}} t) \exp(-i\omega_{\mathrm{R}} t)$. Here ω_{R} corresponds to the true eigenfrequency of VC gyrotropic motion and nonzero values of the imaginary term ω_{I} indicate that the orbital amplitude changes with time as in the form of $\mathbf{X}_0 \exp(\omega_{\mathrm{I}} t)$. From the above results, the orbit radius of the VC motion as a function of time is given as $R_{\mathrm{orb}}(t) = |\mathbf{X}_0| \exp(\omega_{\mathrm{I}} t)$, and the phase relation between X_x and X_y is $X_y / X_x = e^{\pi/2}$, which reflect a circularly rotating motion of a VC inside the dot with ω_{R} and with CCW (CW) rotation sense for $\omega_{\mathrm{R}} > 0$ ($\omega_{\mathrm{R}} < 0$). Therefore, the obtained results from the simulations, shown in Fig. 5.2, can be more quantitatively understood from the analytical equations of ω_{R} and ω_{I} that vary with $p = \pm 1$ and $c = \pm 1$, the magnitude and direction of j_0, and $S_{\mathrm{pol}} = \pm 1$ for the material and the dimensions of a given nanodot.

Moreover, the circumferential OH generated by the flow of out-of-plane currents should be considered to understand how this type field affects both ω_{R} and ω_{I}. As discussed in the previous section (Chapter 4), it is known that the OH influences the variation of κ, such that $\kappa = \kappa_0 + \kappa_{\mathrm{OH}}$, where κ_0 is the intrinsic stiffness coefficient without considering the OH

68

contribution, and κ_{OH} is the additional term newly introduced by the OH contribution to the effective potential energy of a displaced VC. The κ_{OH} term is proportional to j_0 with a constant value of $\eta = ci_{\text{p}}\varsigma$ (where $\varsigma > 0$), so that the sign of η can switch depending on the sign of $c \cdot i_{\text{p}}$. Note that the OH contribution gives rise to the increase (decrease) in κ for the configuration of $c \cdot i_{\text{p}} = +1$ (–1). Based on the "surface charge free" model, ς can be analytically derived in terms of dot dimensional parameters, R and L, and a material parameter, M_{s}, as $\varsigma = \frac{45}{68} RLM_s$.

The Zeeman energy term W_{OH} of a displaced VC due to the OH contribution is expressed as $W_{\text{OH}} = -\mu_0 \int_V dV\, \mathbf{M} \cdot \mathbf{H}_{\text{OH}}$, where $\mathbf{M}$ and $\mathbf{H}_{\text{OH}}$ are the local magnetizations and the Oersted field distribution in the (x, y) plane, respectively. By adopting the "surface charge free" model and the Biot-Savart's formulation, we numerically calculated an analytical form of $W_{\text{OH}} = \frac{1}{2} ci_p \left(\frac{45}{68} RLM_s \right) j_0 |\mathbf{X}|^2 + W_{\text{OH}}(0)$. Comparing this analytical form with $W_{\text{OH}} = \frac{1}{2}\kappa_{\text{OH}} |\mathbf{X}|^2 + W_{\text{OH}}(0)$, we obtain $\kappa_{\text{OH}} = ci_{\text{p}}\varsigma j_0$ and its proportional constant, $\varsigma = \frac{45}{68} RLM_s$ in terms of R, L, and Ms.

Consequently, the ω_{R} and ω_{I} terms are parameterized as:

$$\omega_{\text{R}} = \frac{p\varsigma |G|}{G^2 + D^2} \left[\frac{\kappa_0}{\varsigma} + ci_{\text{p}} j_0 \right],$$

$$(5.3.5)$$

69

$$\omega_{\mathrm{I}} = \frac{B}{G^2 + D^2}\left(j_0 + \kappa_0 \frac{D}{B}\right) \qquad (5.3.6)$$

with $B = ci_{\mathrm{p}}\varsigma D + 2\pi S_{\mathrm{pol}}a_{\mathrm{T}}p|G|$.

For a given dot dimension and a material, ω_{R} and ω_{I} are both controllable with only external driving force parameters, j_0 and i_{p}, for a given vortex state characterized by p and c, and for a given S_{pol}. Here $p \cdot S_{\mathrm{pol}} = +1$ (-1) corresponds to the P (AP) orientation between p and S_{pol}.

For different combinations of $p \cdot S_{\mathrm{pol}} = \pm 1$ and $c \cdot i_p = \pm 1$, we plotted the numerical values (solid lines) of ω_{R} and ω_{I} calculated from equations (5.3.5) and (5.3.6) as a function of the variable j_0, and compared them with the corresponding simulation results (symbols), as shown in Figs. 5.3 and 5.4. The values of ω_{R} and ω_{I} vary with j_0. For $j_0 = 0$ the values of ω_{R} and ω_{I} become $\omega_{\mathrm{R},0} = p\kappa_0|G|/(G^2 + D^2)$ and $\omega_{\mathrm{I},0} = \kappa_0 D/(G^2 + D^2)$, respectively. More specifically, for $p = +1$ ω_{R} increases (decreases) linearly with j_0 for $c \cdot i_p = +1$ (-1), independently of the sign of S_{pol} [see left panel of Fig. 5.3]. In addition, we obtain the relation of $\omega_{\mathrm{R}}(p = -1) = -\omega_{\mathrm{R}}(p = +1)$ [see Fig. 5.3]. Regardless of what signs p and S_{pol} have, for $c \cdot i_p = -1$ there exists a critical value of $j_0 = j_{\max} = -\kappa_0/(ci_p\varsigma)$ where ω_{R} becomes zero, as indicated by the black

70

thick arrows in Fig. 5.3. According to the analytical calculation, the sign of ω_R switches crossing $j_0 = j_{max}$, such that VC gyrotropic motion for a given $p = +1$ (-1) is CCW (CW) in the region of $j_0 < j_{max}$ and switches to CW (CCW) in the region of $j_0 > j_{max}$. However, the numerically estimated value of j_{max} is as extremely large as an order of 10^8 A/cm^2, and hence in such large j_0 values vortex polarization and chirality switching events can take place additionally according to simulation results. Consequently, the analytical results in the region of $j_0 > j_{max}$ are physically meaningless. As we mentioned before, the corresponding simulation results (indicated by symbols) for relatively small values of j_0 are in the same trends as the analytical results, although they show some discrepancies in magnitude.

Instead, as shown in Fig. 5.4, the linear variations of ω_I with j_0 are contrasting and of opposite slope between $p \cdot S_{pol} = +1$ and -1, but their dependence on the sign of $c \cdot i_p$ is ignorable in the region of small j_0 values. For $p \cdot S_{pol} = +1$, $\omega_I < 0$ in the entire region of j_0, which reflects the fact that $R_{orb}(t)$ decreases exponentially with time, as $R_{orb}(t) = |\mathbf{X}_0| \exp(\omega_I t)$, and consequently reaches $\mathbf{X} = 0$. For the other case of $p \cdot S_{pol} = -1$, ω_I linearly increases with j_0, but its sign changes from negative to positive one crossing $j_0 = j_{cri}$ where $\omega_I = 0$. The value of j_{cri} is analytically derived as

$j_{cri} = -\kappa_0 D / B$ with $B = ci_p \varsigma D + 2\pi S_{pol} a_T p |G|$ from equation (5.3.6). It is

clear that for $j_0 < j_{cri}$, $\omega_I < 0$, but for the other region $j_0 > j_{cri}$, $\omega_I > 0$.

The fact of $\omega_I > 0$ implies that $R_{orb}(t)$ exponentially increases with time, as

$|\mathbf{X}_0| \exp(\omega_I t)$. The important point we have to stress here that VC gyrotropic

motions driven by $j_0 = j_{cri}$ are maintained on an initially displaced VC orbit

radius, $|\mathbf{X}_0|$ and with a characteristic value of $\omega_R' = \omega_R (j_0 = j_{cri})$. The

analytical form of ω_R' was obtained to be $\omega_R' = \omega_{R,0} (1 - ci_p \varsigma D / B)$ by

putting $j_0 = j_{cri}$ into Equation (5.3.5). The value of j_{cri} is a crucial parameter

for controlling persistent vortex oscillations by applications of out-of-plane

dc current. For the cases of $j_0 \neq j_{cri}$, the vortex oscillations cannot

persevere because the orbital amplitude either decreases or increases for

those cases. This phenomenon can be applicable to self-sustained vortex

oscillators. Some simulation results (noted by symbols) are in similar trends

with the analytical calculations, but their discrepancy in magnitude becomes

increased with j_0.

It is worthwhile to address more physical pictures on the observed

steady-state vortex oscillations. The oscillation behaviors of **M**s of single-

domains in spin valve structures caused by STT have been understood by

force balance between the STT and the Gilbert damping term. In analogy, we

consider force balance between the Gilbert damping term

72

$\mathbf{F}_D = D\dot{\mathbf{X}} = \omega_R' D(\hat{\mathbf{z}} \times \mathbf{X})$ and $\mathbf{F}_{STT} = 2\pi S_{pol} a_T j_{cri} (\hat{\mathbf{z}} \times \mathbf{X})$ for the condition of $\omega_I = 0$ at $j_0 = j_{cri}$ required for steady-state vortex oscillations. Inserting $j_{cri} = -\kappa_0 D / B$ and $\omega_R' = \omega_{R,0}\left(1 - ci_p \varsigma D / B\right)$ into the two yields $\mathbf{F}_D = -\mathbf{F}_{STT}$, verifying that the steady-state vortex oscillations can maintain at $j_0 = j_{cri}$ in the case where the spin torque force cancels the Gilbert damping force.
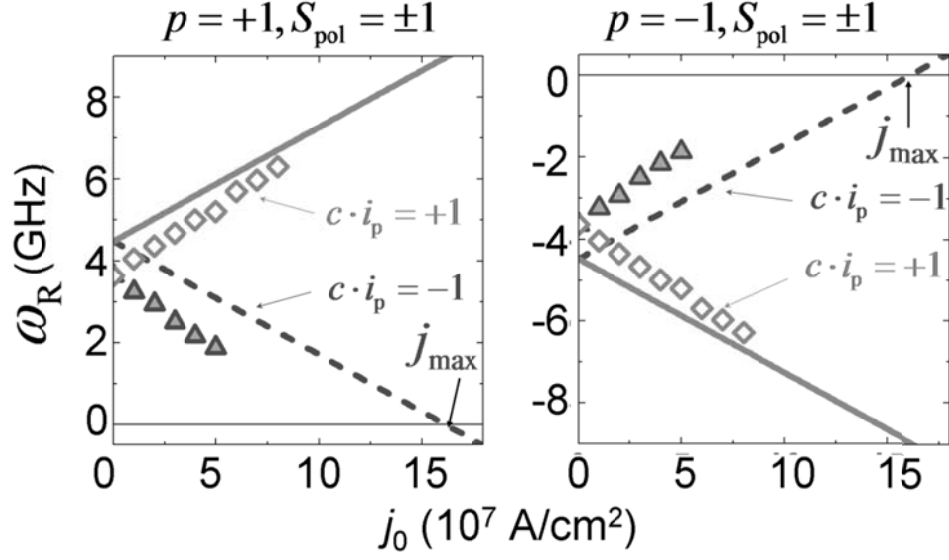
Fig. 5.3 Estimated values of the real (ω_R) terms of the eigenfrequency (ω) versus j_0 for the indicated cases of $p \cdot S_{pol} = \pm 1$ and $c \cdot i_p = \pm 1$. Symbols and solid lines represent the results of micromagnetic simulation and analytical calculations, respectively.
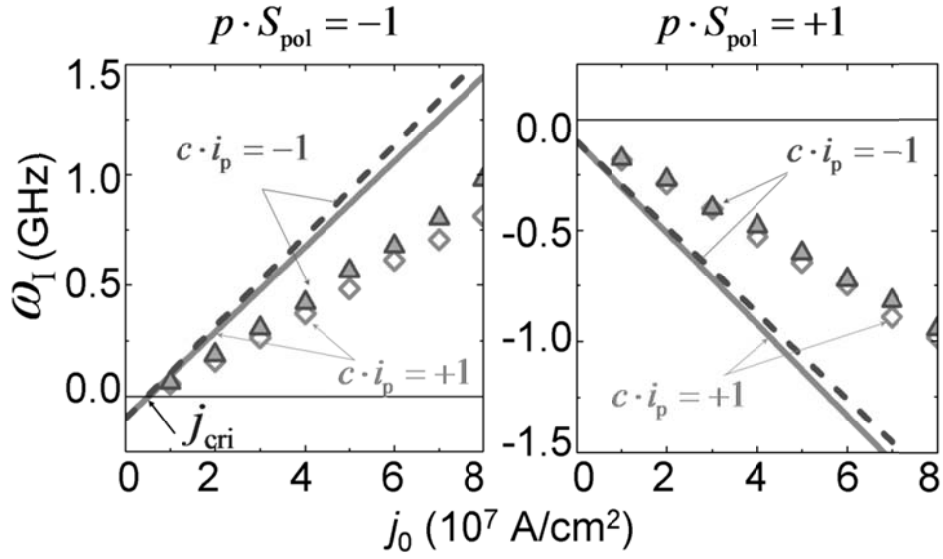
Fig. 5.4 Estimated values of the imaginary (ω_I) terms of the eigenfrequency (ω) versus j_0 for the indicated cases of $p \cdot S_\mathrm{pol} = \pm 1$ and $c \cdot i_\mathrm{p} = \pm 1$. Symbols and solid lines represent the results of micromagnetic simulation and analytical calculations, respectively.

Next, we numerically calculated the values of j_{cri} and ω_R' versus L and R, as shown in Figs 5.5(a) and 5.5(b). In the calculations, we used the analytical forms of $j_{\text{cri}} = -\kappa_0 D / \left(ci_p \varsigma D + 2\pi S_{\text{pol}} p a_T |G| \right)$ and $\omega_R' = \omega_{R,0} \left(1 - ci_p \varsigma D / B \right)$ with an approximated function of $\kappa_0 = \frac{40}{9} \pi M_s^2 L^2 / R$ (Ref. 22). The terms G and D are also given as $G = 2\pi p M_s L / \gamma$ and $D = -\alpha \pi M_s L \left[2 + \ln \left(R / R_c \right) \right] / \gamma$ with the VC critical radius R_c, which of these equations are also functions of L and R (Ref. [48]). The detail calculations of j_{cri} and ω_R' is as follows:

$$j_{\text{cri}} = \frac{-\kappa_0 D}{ci_p \eta D + 2\pi s_{\text{pol}} a_T p |G|}$$

$$= \frac{\dfrac{40}{9} \pi M_s^2 \dfrac{L^2}{R} \times \dfrac{\alpha \pi M_s L}{\gamma} \left(2 + \ln \dfrac{R}{R_c} \right)}{ci_p \dfrac{45}{68} RLM_s \times \dfrac{\alpha \pi M_s L}{\gamma} \left(2 + \ln \dfrac{R}{R_c} \right) + 2\pi s_{\text{pol}} \dfrac{\hbar P}{2\mu_0 e} p \dfrac{2\pi q M_s L}{\gamma}}$$

$$= \frac{\dfrac{40}{9} \pi M_s^2 \dfrac{L^2}{R} \times \alpha \left(2 + \ln \dfrac{R}{R_c} \right)}{ci_p \dfrac{45}{68} RLM_s \times \alpha \left(2 + \ln \dfrac{R}{R_c} \right) + 2\pi s_{\text{pol}} \dfrac{\hbar P}{2\mu_0 e} p 2q}$$

$$= \frac{C_1 \dfrac{L^2}{R} \left(2 + \ln \dfrac{R}{R_c} \right)}{C_2 RL \left(2 + \ln \dfrac{R}{R_c} \right) + C_3} \tag{5.3.7}$$

76

$$\omega'_R = \frac{p \dfrac{2\pi M_s L}{\gamma}}{\left\{\dfrac{2\pi M_s L}{\gamma}\right\}^2 + \left\{\dfrac{\alpha \pi M_s L}{\gamma}\left(2 + \ln\dfrac{R}{R_c}\right)\right\}^2}$$

$$\times \left[\frac{40}{9}\pi M_s^2 \frac{L^2}{R} + ci_p j_{cri}\frac{45}{68}RLM_s\right] \qquad . \qquad (5.3.8)$$

$$= \frac{2p\gamma}{\alpha \pi M_s L(4+\alpha^2)\left(2 + \ln\dfrac{R}{R_c}\right)^2} \times \left[C_1\frac{L^2}{R} + C_2 j_{cri}\right]$$

with $C_1 = \dfrac{40}{9}\pi\alpha M_s^2$, $\quad C_2 = ci_p\dfrac{45}{68}\alpha M_s$, $\quad C_3 = \dfrac{2\pi s_{pol}\hbar Pp2q}{2\mu_0 e}$.

As seen in both Equations (5.3.7) and (5.3.8), the values of j_{cri} and ω'_R are functions of $c \cdot i_p$, so that they vary with the sign of it. The contour plots of j_{cri} and ω'_R on the (L - R) plane allow us to gain technologically useful phase diagrams for designing the dot dimensions and a magnetic material, in order to control persistent vortex oscillations and their eigenfrequencies. As shown in Fig. 5.5(a), the value of j_{cri} increases dramatically with the increasing L for a given R, whereas j_{cri} decreases slowly with increasing R relatively for a constant value of L. The surprising result is that the value of j_{cri} is as extremely low as the order of 10^4 A/cm^2 in the region of $L < 3$ nm. The eigenfrequency obtained at $j_0 = j_{cri}$ varies remarkably with L and R, indicating its tunability, by dot dimensions, in a very broad range from 10 MHz to 2 GHz. We also compare the numerically

estimated values of j_{cri} and $\omega'_{\text{R}}/2\pi$ using the analytical equations with those obtained using micromagnetic simulations for several dot dimensions of [R (nm), L (nm)] = [105, 20], [150, 20], and [150, 10], as shown in Table 5.2. Although there are some discrepancies in the results between the analytical and simulation calculations, their general trends according to L and R are in good agreements.
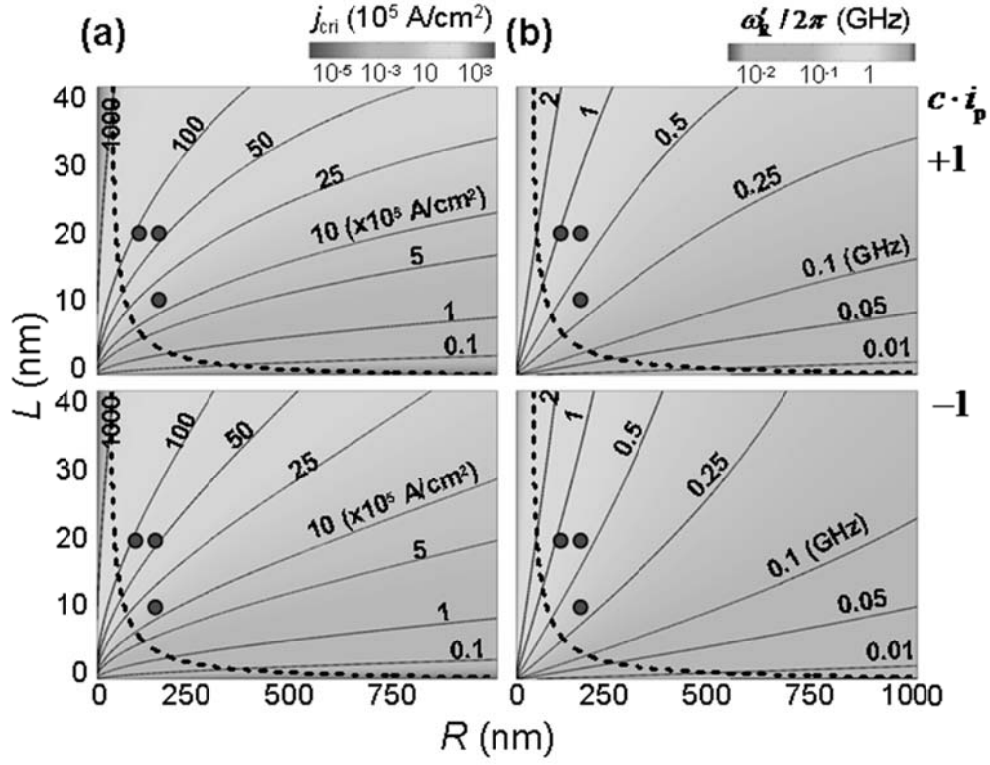
Fig. 5.5 Contour plot of j_{cri} versus dot thickness L and radius R, and plot of $\omega'_R/2\pi$ obtained at $j = j_{cri}$ for both cases of $c \cdot i_p = \pm 1$ and for $p \cdot S_{pol} = -1$. Both j_{cri} and $\omega'_R/2\pi$ were obtained from numerical calculation of the corresponding analytical forms:

$$j_{cri} = -\kappa_0 D / \left(c i_p |\eta| D + 2\pi S_{pol} p a_T |G| \right) \quad \text{and} \quad \omega'_R = \omega_{R,0} \left(1 - c i_p |\eta| D / B \right) \quad \text{with}$$

$\kappa_0 \approx \frac{40}{9} \pi M_s^2 L^2 / R$. The region above the dashed line corresponds to stable vortex states obtained using an analytical equation of P.-O. Jubert et al. [49].

ci_p	Dot size		j_{cri} (10^6 A/cm^2)		$\omega'_R/2\pi$ (GHz)	
	R (nm)	L(nm)	Anal.	Micromagnetic	Anal.	Micromagnetic
+1	105	20	9.29	6.4	1.05	0.83
	150	20	6.21	5.2	0.74	0.61
	150	10	1.47	1.6	0.36	0.34
−1	105	20	8.79	6.1	0.99	0.78
	150	20	5.77	4.8	0.69	0.55
	150	10	1.42	1.5	0.35	0.32

TABLE 5.2. Comparison of the numerical values of j_{cri} and $\omega'_R/2\pi$ between the analytical calculation and micromagnetic simulation results for several dot dimensions, as indicated by the small circles in Fig. 5.5.

Chapter 6

Vortex core switching driven by out-of-plane current

The unique spin configuration of magnetic vortices, which are found in the restricted geometries of magnetic nanodots of various shapes [2] is characterized by an in-plane curling magnetization of either counter-clockwise ($c = +1$) or clockwise ($c = -1$) orientation (denoted by *chirality c*) along with an out-of-plane core magnetization of either upward ($p = +1$) or downward ($p = -1$) orientation (represented by *polarization p*). The combinations of either chirality and either polarization of a vortex, hereafter denoted as $(p, c) = (\pm 1, \pm 1)$, represent the fourfold degenerate states. Thus, the vortex has been regarded as a promising candidate for future high-density nonvolatile memory devices. Moreover, in recent years several groups have demonstrated binary-state p switching by external applications of not only linearly oscillating [39, 46] in-plane fields, circularly rotating [10, 11] in-plane fields but also their pulse forms [45] with lower-power consumption. In addition to such field-driven p switching, it has also been demonstrated that the application of spin-polarized in-plane AC current [22, 24] or out-of-plane DC current[23, 26] is an efficient way to manipulate switching between the binary p states.

Accordingly, based on the fourfold degenerate vortex states and the high thermal stability, several groups proposed different types of binary-digit nonvolatile vortex random access memory (VRAM) [11, 50]. For examples, Kim *et al.* [11] demonstrated a selective switching of the twofold p states of a vortex in an array of dots using circular rotating in-plane fields or currents. Bohlens *et al.* [50] also proposed a different type of VRAM based on alternating in-plane current control of twofold handedness ($c \cdot p = \pm 1$: represented by the product of c and p), as a bit representation, in a specific array of vortex cells and addressing electrodes.

Here, we raise a further issue: if both p and c switchings in a nanodot are controllable in a certain simple way, it would be possible to make a *quaternary-digit* nonvolatile memory device without any loss of the fourfold degree of freedom of a vortex-state dot. A reliable control of switching between each of quaternary vortex states has not been explored so far, although studies on only p switching[10, 11, 22, 24, 26, 39, 45] or only c –switching [51, 52] have been reported. Note that here we exclude studies on chirality (flux closure) switching in nanorings because such rings do not have out-of-plane magnetizations as in vortex-core areas. In this section, we report the results of micromagnetic numerical simulations of out-of-plane-current-controlled switching between the fourfold degenerate vortex states. We also present a promising means of manipulating individual switching

82

from each of the four states to any of the other states as well as back again, using different sequence combinations of the characteristic single-step current pulses, as found from this study.

6.1 Simulation conditions

We used Permalloy (Py, $Ni_{80}Fe_{20}$) cylindrical dots, each of a different radius in the range of $R = 50 \sim 100$ nm and a different thickness of $L = 5 \sim 50$ nm, as shown in Fig. 1. The initial ground state was either $(p, c) = (+1, +1)$ or $(p, c) = (+1, -1)$. In order to conduct the model study of spin-polarized out-of-plane current-driven vortex excitations in the free-standing dots, we assumed that the spin polarization points in the $-z$ direction, (i.e. $S_{pol} = -1$), along with the degree of spin polarization $P = 0.7$ [see Fig. 6.1(a)]. The current flow was in the $+z$ direction (denoted as $i_p = +1$). The circumferential Oersted fields due to the current flow were taken into account using Biot-Savart's formulation [53]. We numerically calculated the magnetization dynamic motions of individual unit cells (size: $2 \times 2 \times L$ nm^3) using the OOMMF code [54] that employs the Landau-Liftshitz-Gilbert equation [35], including the so-called Slonczewski spin-transfer torque (STT) [12].
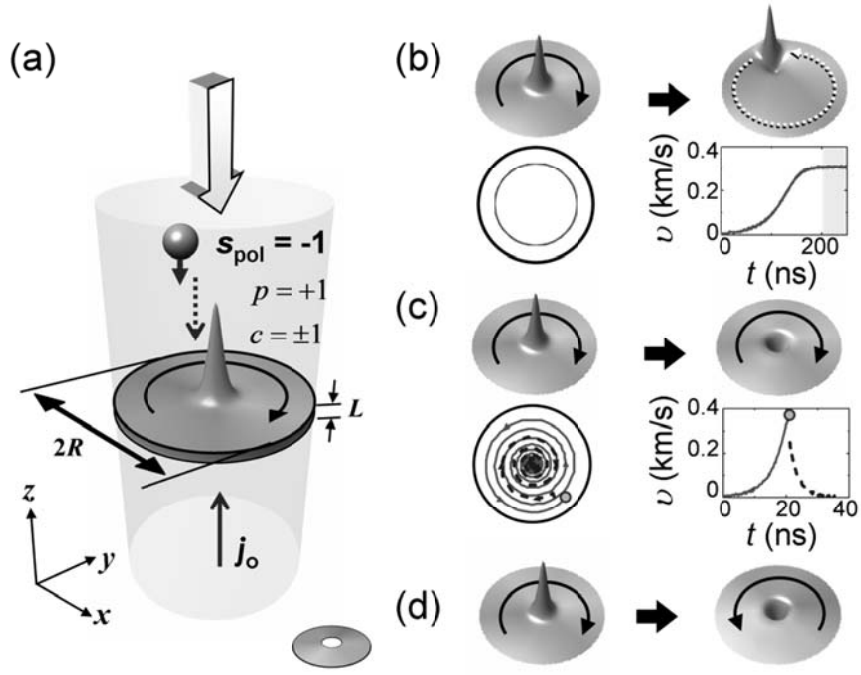
Fig. 6.1 Schematic illustrations of (a) the model geometry and (b) the magnetic vortex states used. The directions of the out-of-plane current and the spin polarization of the electrons are denoted as $i_p = +1$ and $S_{pol} = -1$, respectively, as shown in illustration (a). The colors and the height of the surface shown in (b) correspond to the in-plane and out-of-plane components of the local magnetizations, respectively.

6.2 Various switching behavior by the amplitude of current density

The simulation results on specific dot dimensions, e.g., $(R, L) =$ (100 nm, 17 nm) and the indicated initial state, $(p, c) = (+1, -1)$ are shown in Fig. 6.2, which diagrams the switching of p alone and the simultaneous switching of both p and c, as well as the vortex motion and no further excitation in different regimes of the current density j_0. Note that, with this initial vortex state, the circumferential OH orientation is antiparallel with the $c = -1$ orientation and the $p = +1$ orientation is parallel with the current direction, $i_p = +1$. The switchings from the $(p, c) = (+1, -1)$ state contrasted with the different j_0 regions, as shown in Fig. 6.2. In fact, the observed vortex excitations could be classified into three different regimes with respect to the j_0 value, except for "no further excitation" in regime I_0 (j_0 below a certain critical density, j_{cri}). In regime I ($j_0^{cri} < j_0 < j_0^{I-II}$), such vortex excitation is the low-frequency translation mode, the so-called vortex gyrotropic motion [7, 53, 55]. In this regime, the vortex core exhibits a spirally rotating motion with a continuously increasing orbital radius, finally attaining the stationary motion of a constant orbital radius along with the eigenfrequency ω_R. In regime I, therefore, only the vortex gyrotropic motions are observed without any p and/or c switchings.

86

In contrast to the earlier I_0 and I regimes, in regime II ($j_0^{\text{I-II}} < j_0 < j_0^{\text{II-III}}$), only p switching occurs, maintaining the initial state of $c = -1$ (without c-switching), after the application of the DC current of the required p-switching duration time. The switching time, indicated by the solid circles and line, decreases with increasing j_0. For the lower j_0 values in regime II, the p-switching takes place via the creation and annihilation of a vortex-antivortex pair inside a given dot, according to the same mechanism and origin as described in earlier studies [10, 39, 45]. It was also confirmed that the critical velocity, as the criterion for p-switching, is 330 ± 37 m/s, which is the same as that driven by oscillating in-plane and circular rotating fields (or currents) [10]. However, for the higher j_0 values in regime II, the p-switching mechanism differed from that observed in the lower j_0 region.

With further increases of j_0 across $j_0^{\text{II-III}}$, an additional vortex dynamic was found that represents the switching of both p and c with certain time intervals of the order of ~ ns (hereafter denoted as "p-PLUS-c" switching). In this regime ($j_0 > j_0^{\text{II-III}}$), compared with the earlier regimes, the j_0 values are large, producing high-strength OHs, e.g., 1.25 kOe at $j_0 = 2.0 \times 10^8$ A/cm^2 for $R = 100$ nm. Thus, the high-strength OH assists such "p-PLUS-c" switching via the reduction of the Zeeman energy through the additional c-switching from the antiparallel to the parallel orientation between the c-state and the given OH. Note that such additional c switching

87

never happens for the initial state of $c \cdot i_\mathrm{p} = +1$, as shown in the left and right graphs of Fig. 6.3. However, the switching mechanism is not simple, but different from the field driven magnetization reversals typically observed in ring-type elements [52]. Further simulations results show that the chirality switching by only the OH (without STT effect) occurs above $j_0 = 1.8 \times 10^8$ A/cm^2, which value is six times greater than the threshold value, $j_0^{\mathrm{II\text{-}III}} = 0.3 \times 10^8$ A/cm^2, calculated with considering both the STT and OH effects.
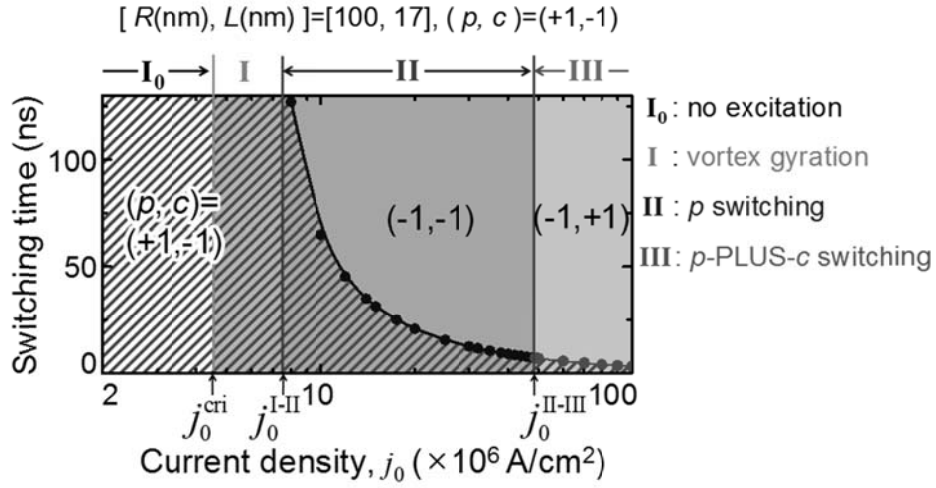
Fig. 6.2 Diagram of no excitation, vortex gyration, "*p*" and "*p*-PLUS-*c*" switching with respect to j_0, as indicated by regimes, I_0, I, II, and III, respectively. The closed symbols indicate the time required for each switching at a given value of j_0. The vertical lines represent the boundaries between the different vortex excitations, corresponding to the threshold j_0 values (j_0^{cri}, j_0^{I-II}, j_0^{II-III}) that distinguish each switching regime. The dot size and vortex state are $[R, L] = [100$ nm, 17 nm] and (p, c) = (+1, −1), respectively, as noted. The hatched area corresponds to the initial ground state before "*p*" and "*p*-PLUS-*c*" switching.
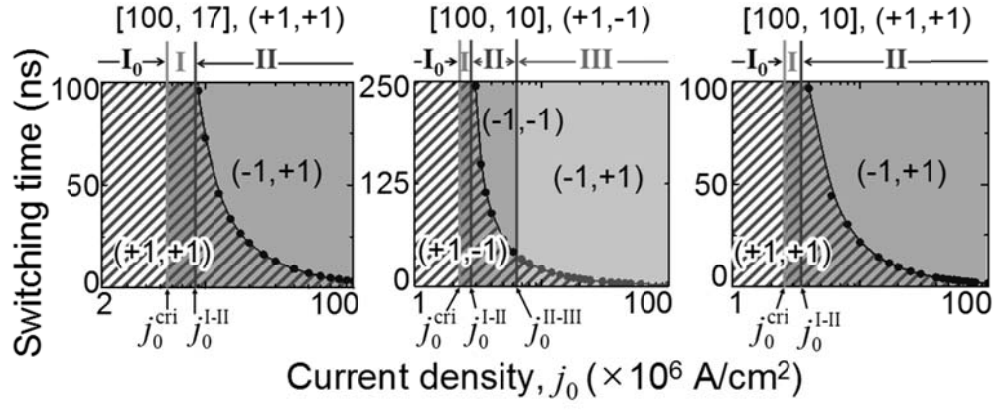
Fig. 6.3 Switching diagrams for the indicated different dot sizes and vortex states. The hatched area corresponds to the initial ground state before "*p*" and "*p*-PLUS-*c*" switching.

6.3 Geometry dependence of critical current density

Next, from an application perspective, it is necessary to construct phase diagrams of the observed characteristic switchings with respect to the dot dimensions and the initial vortex state, as well as the value of j_0. Figure 6.4 shows the phase diagrams on the (j_0 - L) plane for the different R values, (e.g., $R = 50$, 75, and 100 nm). For $c = +1$, c-switching never occurs, since, as addressed earlier, its direction is parallel to that of the circumferential OH, and thus only the p-switching regions are present. By contrast, for the other state, $c = -1$, there exist both "p" and "p-PLUS-c" switchings (noted as II and III, respectively), along with their clear boundaries. Note that as L decreases, the value of $j_0^{\text{II-III}}$ reduces and then converges to zero. This result is promising from a technological point of view. When L decreases and R increases until maintaining stable vortex states, for example, the $j_0^{\text{I-II}}$ and $j_0^{\text{II-III}}$ values decrease to 3.0 and 7.0×10^6 A/cm^2, respectively, for (R, L) = (100 nm, 10 nm). Moreover, the value of $j_0^{\text{II-III}}$ further decreases down to 9.0×10^5 A/cm^2 for (R, L) = (1000 nm, 10 nm). In practical applications, the reduction of the current density and scalability are both crucial, thus these need to be reconciled.
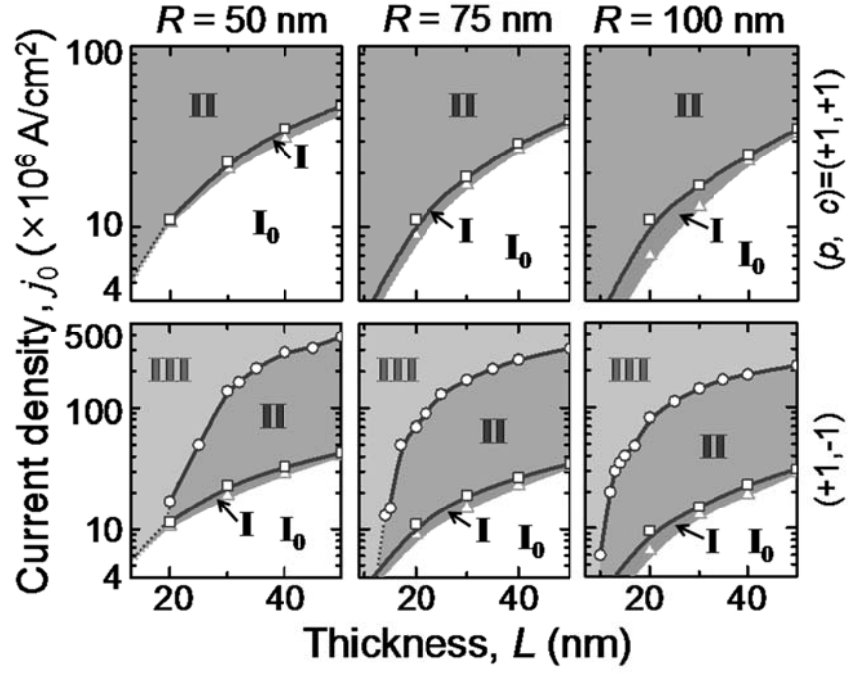
Fig. 6.4 Phase diagrams of different "*p*" and "*p*-PLUS-*c*" switching regimes, including vortex gyration and no excitation regimes, with respect to the *L* and j_0 for the several *R* values of, e.g., *R* = 50, 75, and 100 nm, and for the two different states, $(p, c) = (+1, +1)$ and $(p, c) = (+1, -1)$. The individual regions are marked by different colors and the same symbols, I_0, I, II, and III, as employed in Figs. 6.2 and 6.3.

6.4 Conceptual design of multi-bit random access memory

On the basis of the previous results, we propose a promising means by which the individual vortex states can be simply but reliably manipulated, which method can be implemented for information recording in a potential quaternary-digit nonvolatile memory device. In Fig. 6.5 (a), we schematically illustrated ten different pulse sequences composed of single-, double- or triple-step pulses. Each current pulse is of either density value, $j_0^{\text{I-II}} < j_0 < j_0^{\text{II-III}}$ or $j_0 > j_0^{\text{II-III}}$, and either current direction, $+z$ or $-z$. The lengths of the step pulses are supposed to be at least longer than the switching times, t_{p} (10 ~ 250 ns) and $t_{\text{p+c}}$ (< 30 ns), required for "p" and "p-PLUS-c" switchings, respectively. For example, for p switching, single-step pulses with t_{p}, (pulse types ① and ②), are necessary. Here, the current density and length of the step pulses were determined by the dot dimensions and vortex states, as shown in Figs. 6.2, 6.3, and 6.4. Contrastingly, c-state switching can be achieved only by combining the two different processes of "p-PLUS-c" and "p" switchings, in order to return the p-state to its original state, since c-switching never occurs alone, but occurs along with p switching. The pulse types, ⑤, ⑥, ⑦, and ⑧ effect c-switching. The pulse sequences for "p-PLUS-c" switching are relatively complex: the

93

single-step pulses of ③ and ④ are required for switching between (p, c) = $(+1, -1)$, and $(-1, +1)$, but for switching between (p, c) =$(+1, +1)$ and $(-1, -1)$, the triple-step pulses of ⑨ and ⑩ are necessary. The reason is that the latter switching can occur only through the serial processes of switching from the given $(-1, -1)$ state to $(+1, -1)$ and $(-1, +1)$, and then to $(+1, +1)$, or vice versa. Thus, the pulse sequences ⑨ and ⑩, are the results of the combinations of ①+④+① and ②+③+②, respectively. Consequently, each vortex state can be switched to any of the other states directly through two different processes of the "p" and "p-PLUS-c" switching or their combinations, by one of the pulse sequences indicated by the arrows and the numbers noted in Fig. 6.5. The ten types of pulse sequences shown in Fig. 6.5 were also demonstrated for the "p" and "p-PLUS-c" switchings for another conditions while holding $p \cdot S_{pol} = -1$. With the other conditions for $p \cdot S_{pol} = +1$, there were neither gyrotropic motion and nor any switching.

94
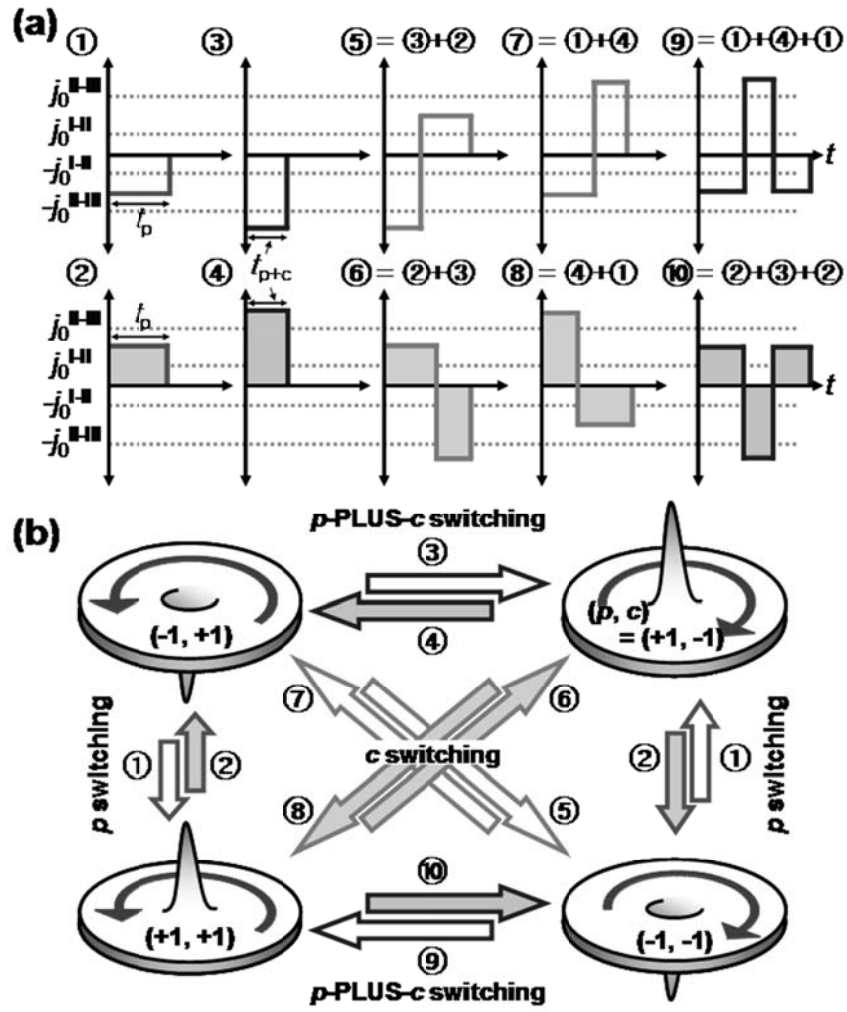
Fig. 6.5 (a) Current pulse sequences (comprised of single, double or triple pulses) required for individual switching between each pair of the quadruple vortex states shown in (b).

Chapter 8

Summary

In this thesis, we investigated the magnetic vortex dynamics in soft magnetic nanoelements under spin-polarized currents, such as gyrotropic motion of vortex core and switching among four degenerated vortex states. To understand the underlying mechanism of these nontrivial dynamics of the vortex structure, we conducted not only micromagnetic simulations with OOMMF code and LLG micromagnetic simulator, but also analytical calculations based on Thiele's equation of motion.

Under in-plane ac currents of different amplitude and frequency in Permalloy nanodots, we found occurrences of current-driven vortex-core reversal and accompanying spin-wave emission. This phenomenon occurred through the creation of a vortex-antivortex pair and subsequent annihilation of the initial vortex and created antivortex. It was found that strong spin waves are emitted in the course of the above serial processes and immediately after vortex core switching. These results provide physical insight into how and when current-driven vortex core switching takes place, thereby offering a means to manipulate bi-state vortex core orientations.

We observed sizable eigenfrequency shifts in vortex gyrotropic motions driven by the out-of-plane spin-polarized dc current and clarified

the underlying physics through micromagnetic numerical calculations. It was found that the vortex eigenfrequency is changed to higher (or lower) values with increasing Oersted field strength associated with the out-of-plane dc current density for the vortex chirality parallel (or antiparallel) to the rotation sense of the Oersted field circumferential in-plane orientation.

In addition, we numerically and analytically calculated the dependences of the eigenfrequency and the orbital radius amplitude of the translation motion of a vortex core in soft magnetic nanodots driven by spin-polarized out-of-plane dc currents. We found some key parameters to reliably control the persistent vortex oscillations, including the vortex eigenfrequency and orbital amplitude. Using the analytically derived equations of the critical current density for persistent vortex motions and their eigenfrequencies, we constructed two phase diagrams of the critical current density and eigenfrequency on the plane of dot thickness and radius for a Permalloy material. These results provide guidance for practical implementation of vortex oscillations in nanodots to a new class of oscillator with tunable eigenfrequency in a broad range, with high q-factor, and extremely low current densities, as small as $10^4 \sim 10^5$ A/cm^2.

Finally, we studied the dynamic switching of both polarization and chirality of the fourfold degenerate vortex states in soft magnetic dots by applying spin-polarized out-of-plane dc or pulse currents of different densities and directions. It was found that dynamic switching can be

97

manipulated simply by changing the current density in accordance with the initial ground state and the dot size. The proposed pulse sequences of combinations of four characteristic single-step pulses can affect individual switching from each vortex state to any of the other states. This work opens up the possibility of implementing the full degree of freedom of the fourfold degenerate vortex states in a future quaternary-digit nonvolatile memory device, although further studies of not only the scaling issue but also temperature and defect effects on the switching characteristics are necessary for practical applications.

Appendix

A. Experiment results

In this thesis, we discussed the vortex dynamics driven by out-of-plane spin-polarized dc current using analytical calculations and micromagnetic simulations. In this section, we tried to observe the vortex dynamics, especially the critical current density for exciting the vortex core oscillation, by measuring the output signal from an electrical measurement system with giant-magneto-resistance (GMR). Unfortunately, the experiment failed. As this is an ongoing experiment in our laboratory, we are reporting the experimental setup such as the environment, sample fabrication processes, results, and also propose directions for future work.

1 Experiment environment

The complicated multilayer samples were deposited using a cluster chamber system. This system consists of the following: 1) an E-beam evaporation chamber with an in-situ surface magneto-optical Kerr Effect, 2) a DC sputtering chamber for depositing Py and Exchange bias, 3) a DC sputtering chamber for depositing Cu, 4) an RF sputtering chamber for

depositing MgO, 5) a pre-chamber, 6) a transfer chamber for transferring samples among the above chambers, and 7) a pulsed laser deposition chamber (PLD). Each chamber involves independent electronics, pumps and gas handling lines, and are isolated by gate valves. In this experiment, we used the E-beam evaporation chamber, two DC sputtering chambers, the pre-chamber, and transfer chamber. The entire shape of the cluster chamber system is shown in Fig. A.1.
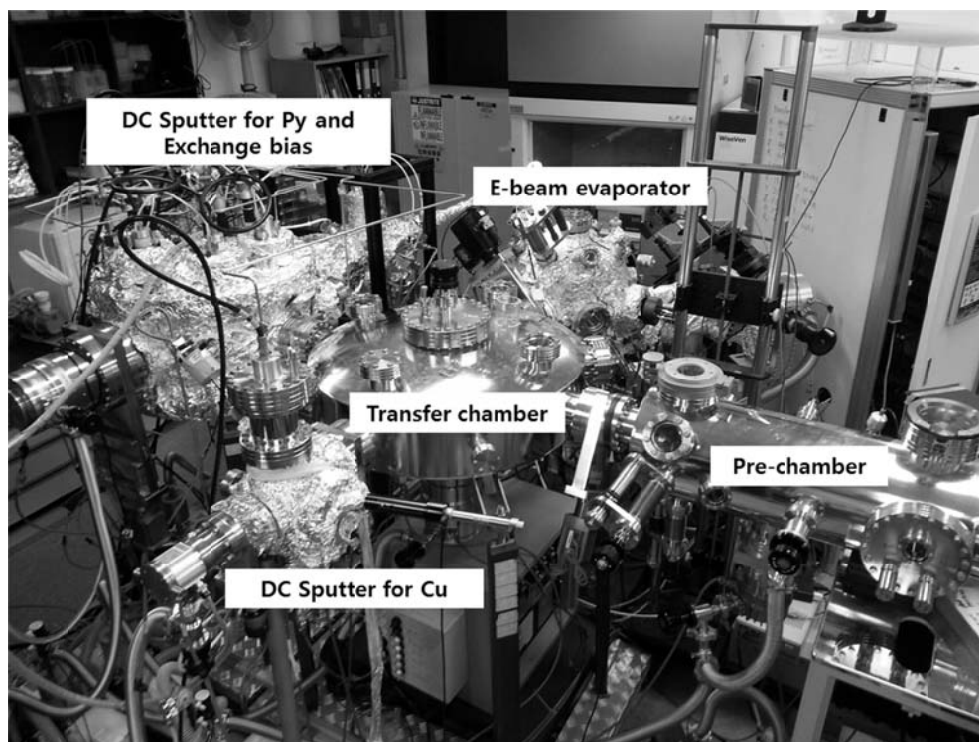
Fig. A.1 Picture of the cluster chamber system

1.1 E-beam evaporation chamber

The E-beam evaporation chamber is composed of four electron-beam evaporators (EFM4, Omicron) in which an integral flux monitor enables reproducible real-time control of the deposition rate. (Fig. A.2) Highly efficient water-cooling ensures negligible outgassing during operation, thus the chamber pressure is maintained at an ultrahigh-vacuum (UHV) condition, typically below 1×10^{-9} Torr. The precisely defined evaporation beam allows for a highly uniform deposition area on the sample. The deposition area is determined by the aperture and the distance from the source to the sample. In our experimental setup, the uniform deposition area is about 50 mm at the distance of 120 nm with the aperture diameter of 10 mm.

We can measure the Kerr signal using the surface magneto-optical Kerr effect (SMOKE) in the E-beam evaporator chamber. (Fig. A.3) We used the photo-elastic modulator (PEM-90, Hinds Instruments) as a precision compensator. This provides dynamic phase retardation of the elliptically polarized light from the sample. In this way, we can obtain magneto-optical properties through phase-sensitive detection with high accuracy ($\sim 0.001°$), instead of by mechanical rotation of an analyzer. As a light source and detector, a red He-Ne laser (R-30993, Newport) and a photodiode detector unit (DET-90, Hinds Instruments) are used. The red He-Ne laser generates a 500:1 linearly polarized output of 12.0 mW at 633

nm. The laser light incidents to the electron-beam evaporation chamber through fused quartz windows (#450020, MDC), which minimize perturbation of the laser polarization state. For polarizing optics, Clan-laser calcite polarizers (10GL08AR.14, Newport) are used. This polarizer provides an extinction rate better than 10-5 in the wavelength range of 400-1064 nm with unpolarized input. This polarizer also has broadband visible antireflection coating in the 430-700 nm wavelength range. For alignment of the sample in the UHV chamber, the chamber is equipped with a manipulator (HPT translator, Thermo Vacuum Generators) and a specially designed sample holder (XL25HC sample handling system, Thermo Vacuum Generators), as shown in Fig. A.4. The manipulator provides for x, y, and z motions of the sample with a resolution of 5 um. Additionally, the sample can be rotated in the primary and azimuthal directions by the manipulator's rotary drive. For accurate SMOKE measurements, the sample holder consists of low-magnetic materials such as the molybdenum sample plate, the beryllium copper bearing, and the alumina isolators.

Fig. A.2 Picture of the E-beam evaporation chamber.
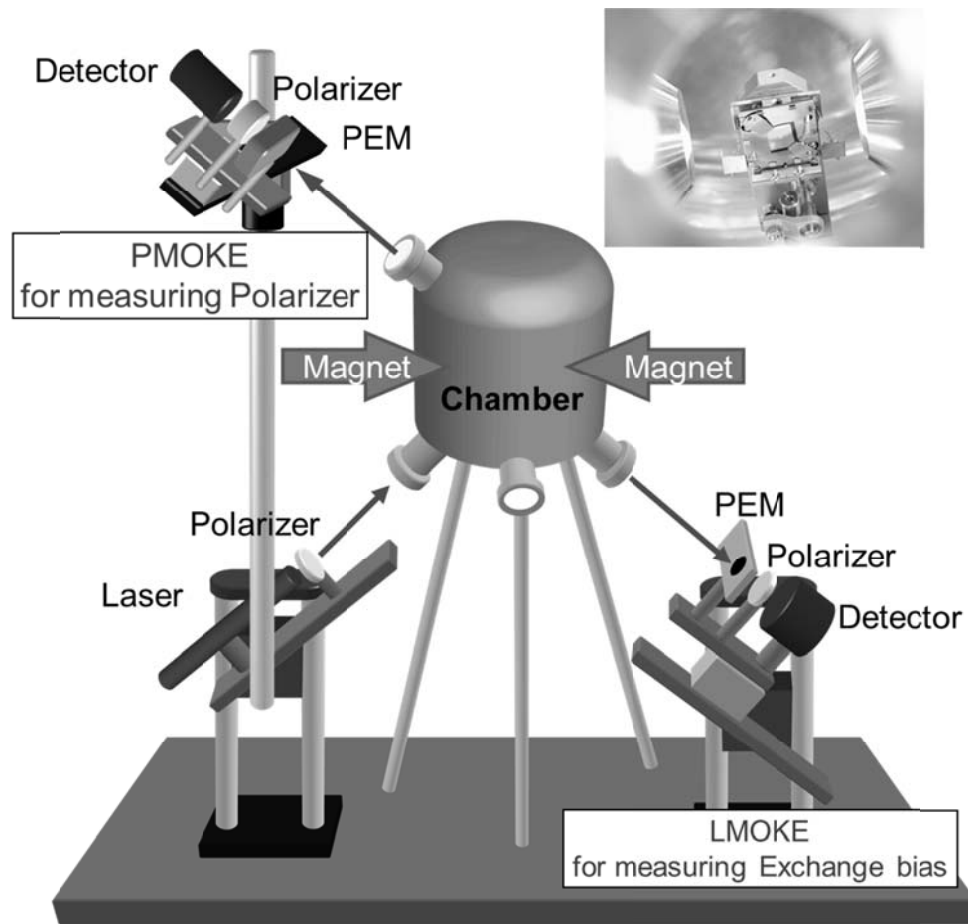
Fig. A.3 Schematic feature of surface magneto-optical Kerr effect (SMOKE) system [56]
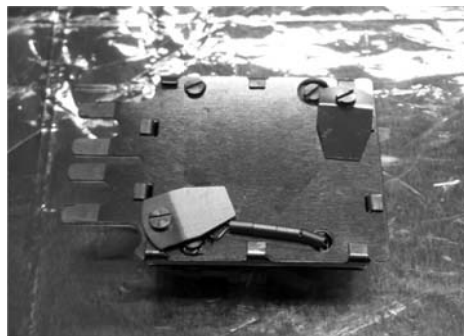
Fig. A.4 Picture of the specially designed sample holder (XL25HC).

1.2 DC sputtering

Sputter deposition is a physical vapor deposition (PVD) method that ejects atoms from target materials, which then attach to a substrate. By first creating gaseous plasma and accelerating the ions from this plasma into the target material, the target material is eroded by the arriving ions via energy transfer, and is ejected in the form of neutral particles, either individual atoms, clusters of atoms or molecules. As these neutral particles are ejected, they will travel in a straight line unless they come into contact with something, whether other particles or a nearby surface. If a substrate is placed in the path of these ejected particles, it will be coated by a thin-film of the source materials.

The cluster chamber system has three chambers for DC and RF sputtering of metals and dielectrics from 2-inch targets. In this experiment, we used only two DC sputtering chambers. The background pressure of the sputtering chamber is lower than 2×10^{-9} Torr, and is maintained using turbo molecular pumps backed by rotary vane pumps. The substrates are mounted on a rotation stage, and can be positioned directly under the sputter sources in a parallel source-substrate configuration. The distance between the sputter source and the substrate can easily be controlled. The argon gas flow for the sputtering procedure is automatically controlled by mass flow controllers (MFCs) and gate valves. Heating of the substrate to 700°C is possible by means of a heating-lamp module.

106
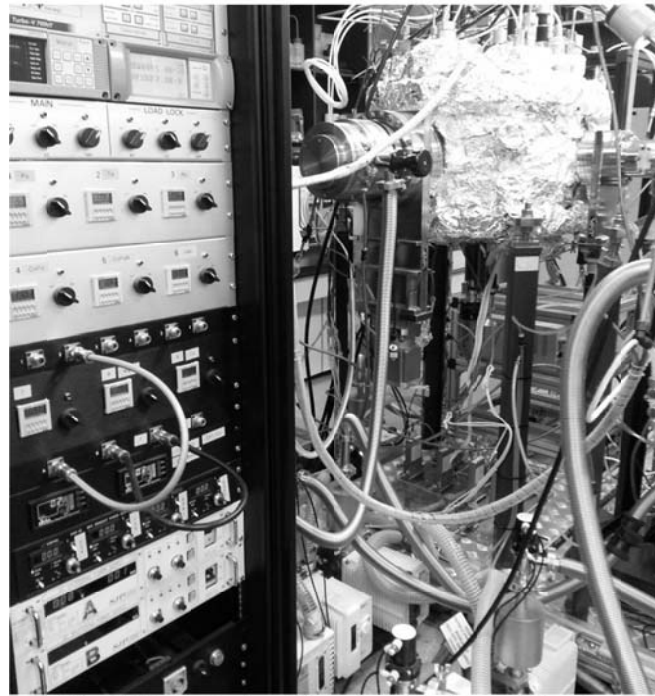
Fig. A.5 Picture of the DC sputtering Chamber for Py and Exchange bias
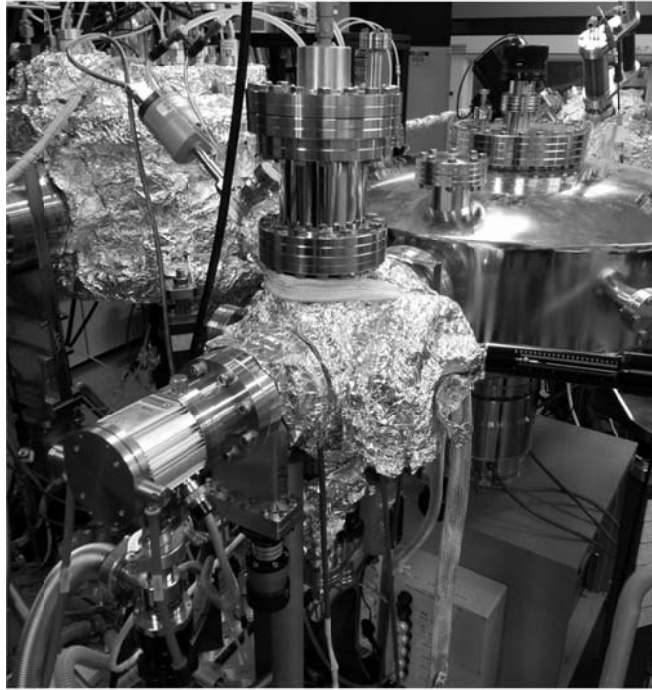
Fig. A.6 Picture of the DC sputtering Chamber for Cu.

2 Sample preparation

The fabrication process in this thesis can be classified into two parts: magnetic material deposition and patterning process. The patterning process and electrode deposition in the fabrication processes are performed at the Korea Advanced Nano Fab Center (KANC) in the city of Suwon, Gyeonggi, South Korea. This facility has cleanliness from 1,000 to 1 class. The deposition of magnetic materials is performed using our cluster chamber system. The complicated fabrication process is described in Fig. A.7 and A.8.
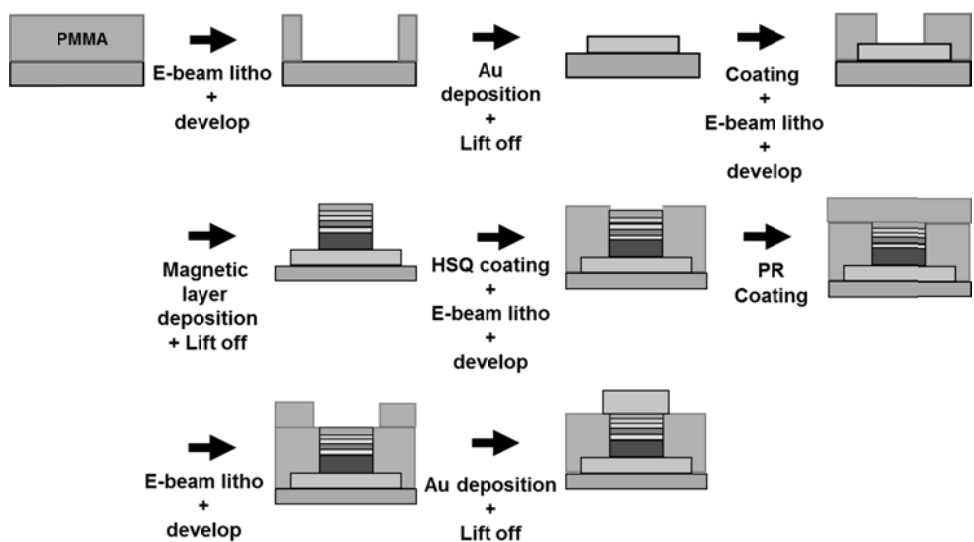
Fig. A.7 Fabrication process flow of the sample preparation. (Side view)
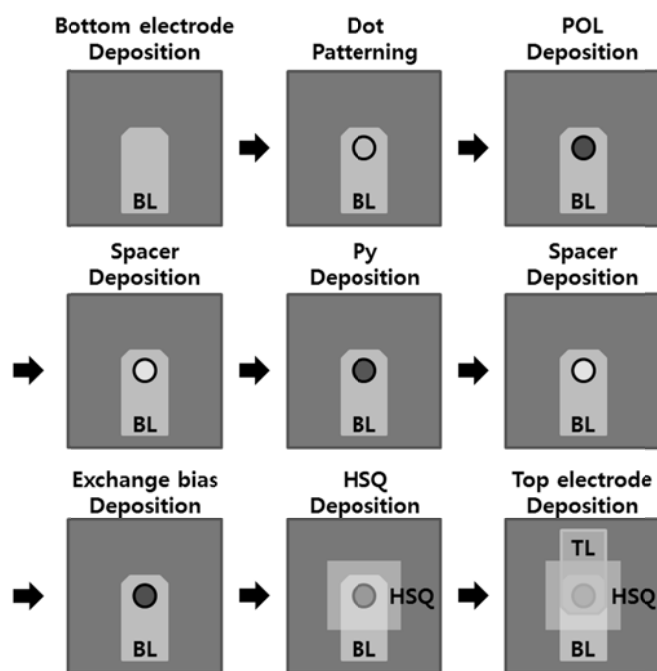
Fig. A.8 Fabrication process flow of the sample preparation. (Top view)

For patterning a **bottom electrode**, a resist layer (400 nm-thick ZEP-520A) was spin-coated at a speed of 3000 rpm onto the silicon wafer substrate. At 170°C, the ZEP-520A was prebaked on a hotplate for 300 sec. Then, the electron-beam exposure was carried out with an electron-beam lithography (JBX 6000, Jeol) operating at 50 kV and providing beam currents at 1 nA. The exposure dosage was varied from 100 to 200 uC/cm^2. After e-beam patterning, the exposed ZEP-520A was developed by ZED-N50 for 90 sec and then rinsed in IPA, followed by blow-drying with nitrogen gas. After the development, thin-film Au was deposited onto the pattern by DC sputtering at KANC, and lift off the unpatterned ZEP-520A resist by ZDMAC. IPA and de-ionized water were used for rinsing and cleaning. The lift-off method offers advantages to the processes of patterning difficult-to-etch metal thin films such as platinum, tantalum, nickel, and iron. Typically, this method proceeds as follows: 1) a film is deposited over all of the patterned substrate; 2) the resist under the film is removed by solvent with the film deposited on the resist; 3) the patterned film remains only on the substrate.

Next, we patterned **magnetic disk** of diameter $2R = 500$ and 1000 nm using the resist layer (150 nm-thick PMMA 95KA3) spin-coated at a speed of 3000 rpm. The PMMA was prebaked on a hotplate at 170°C for 300 sec. Then, electron-beam exposure was carried out with the same condition of bottom electrode. After e-beam patterning, the exposed PMMA

was developed by MIBK+IPA (MIBK 1 : IPA 1) for 90 sec and then rinsed in IPA, followed by blow-drying with nitrogen gas. After the development, the magnetic layers were deposited onto the pattern by DC sputtering. The magnetic disk composed of a polarizer, free layer, and fixed layer. The polarizer consisted of CoPd multilayer, Pd (5 nm) / [Co (0.5 nm) / Pd (1.5 nm)]$_3$. The free layer and fixed layer consisted of Py (10 nm) and the exchange bias [CoFe (3 nm) / IrMn (15 nm)], respectively. To prevent the exchange coupling between the polarizer, the free layer, and the fixed layer, the spacer (Cu 3nm) was deposited between each layer. The deposition condition of the polarizer and exchange bias was optimized by SMOKE measurement. (Fig A.9 - A.11)

Before patterning a top electrode, **HSQ layer** (100 nm-thick XR-1541-006) was patterned for insulating between the bottom and top electrodes. The HSQ layer was spin-coated at a speed of 4000 rpm onto the silicon wafer substrate. At 110°C, the HSQ layer was prebaked on a hotplate for 60 sec. Then, electron-beam exposure was carried out under the same conditions of bottom electrode. After e-beam patterning, the un-exposed HSQ layer was developed by MF312CD38 for 60 sec and then rinsed in DI water for 30 sec, followed by blow-drying with nitrogen gas.

Finally, **the top electrode** was patterned by the same process with the bottom electrode. The total stack of the sample is Ti (10 nm) / Au (60 nm) / Pd (6.5 nm) / [Co (0.65 nm) / Pd (1.9 nm)]$_3$ / Cu (3 nm) / Py (10nm) /

Cu (3 nm) / CoFe (3 nm) / IrMn (15 nm) / Ta (2 nm) / Ti (10 nm) / Au (200 nm). (Fig. A.12) Tantalum was used for the capping layer to prevent the sample oxidation and Titanium was used for adhesion between the silicon substrate and electrodes (Au).
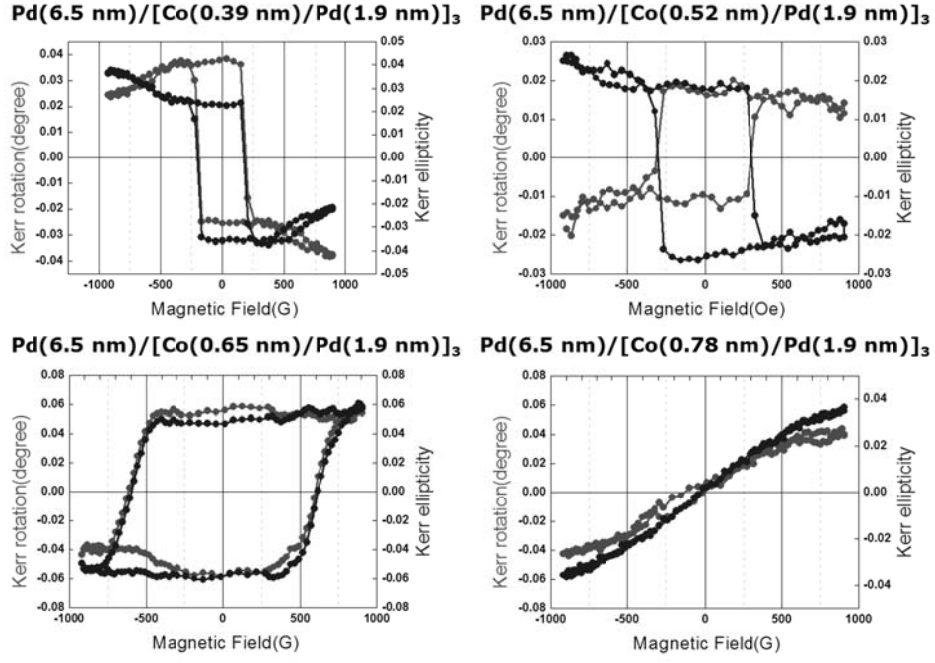
Fig. A.9 Perpendicular Kerr rotation result of the polarizer according to the Co thickness.
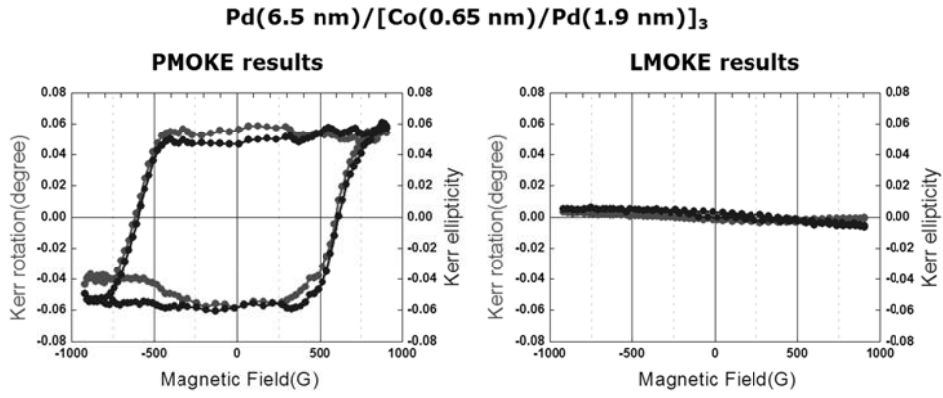
Fig. A.10 Perpendicular (left) and Longitudinal (right) Kerr rotation result of the polarizer according to the Co thickness.
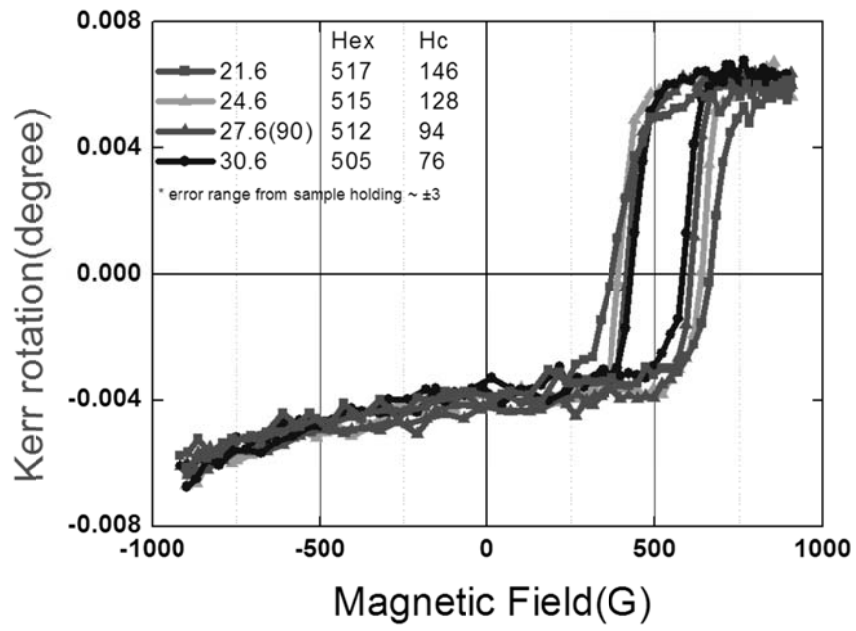
Fig. A.11 Longitudinal Kerr rotation result of the exchange bias [Cu (3 nm) / CoFe (3 nm) / IrMn (15 nm) / Ta (2 nm)] according to the rotation angle of the stage.
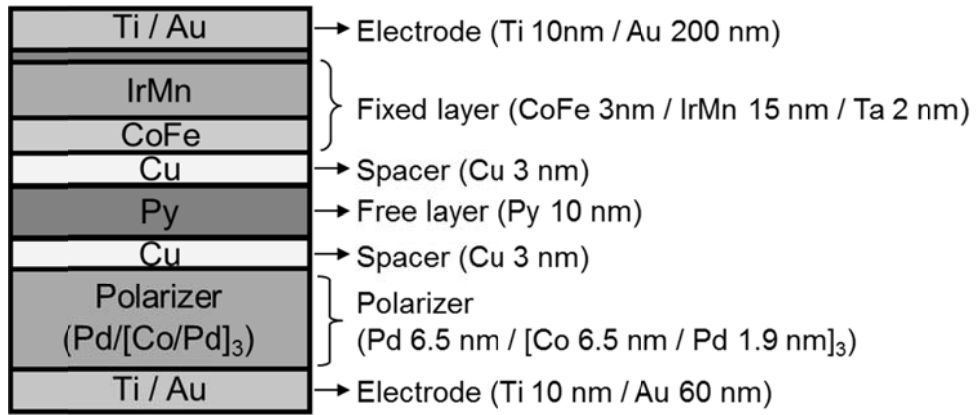
Fig. A.12 Side view of the sample geometry. In this view, the HSQ layer is not considered. Actually, the HSQ layer is covered between the bottom and top electrodes except the above magnetic nanodot layer.

3 Experiment results and future work

The schematic illustration of our electrical measurement setup is shown in Fig. A.13. Each system (pulse generator, probe station, and oscilloscope) is connected by SMA connectors, and two dc probes are contacted on the electrodes of the patterned sample as shown in Fig. A.15. We applied the input current pulse using the pulse generator, where the total duration time is 2.0 μs, the raising edge 1.0 μs, and the end edge 2.5 ns. (Fig. A.16) We used long raising edge to prevent the overshoot of the current pulse. The applied current pulse is passed through the sample, and the output signal can be measured using the oscilloscope. The analytically calculated critical current (critical voltage) using the previous results in Section 5 was 2.4 mA (120 mV). The impedance of the pulse generator and oscilloscope were 50 Ω and 1MΩ, respectively.

We expected the following result. When the vortex core is excited by the critical current as we mentioned in the previous sections, the value of the magneto-resistance will be changed periodically with the same frequency of the VC gyration. As a result, the output signal will be oscillated with the same frequency of the VC gyration.

In this experiment, however, we could not measure the oscillated output signal because the current pulse did not pass through the sample. To

solve this problem, we are going to observe the cross-section of the sample using Transmission Electron Microscope (TEM). After this observation, we expect other graduate students in our laboratory to solve the problems and fabricate new samples. Finally, we expect them to measure the critical current for vortex core oscillation using an electrical measurement setup.
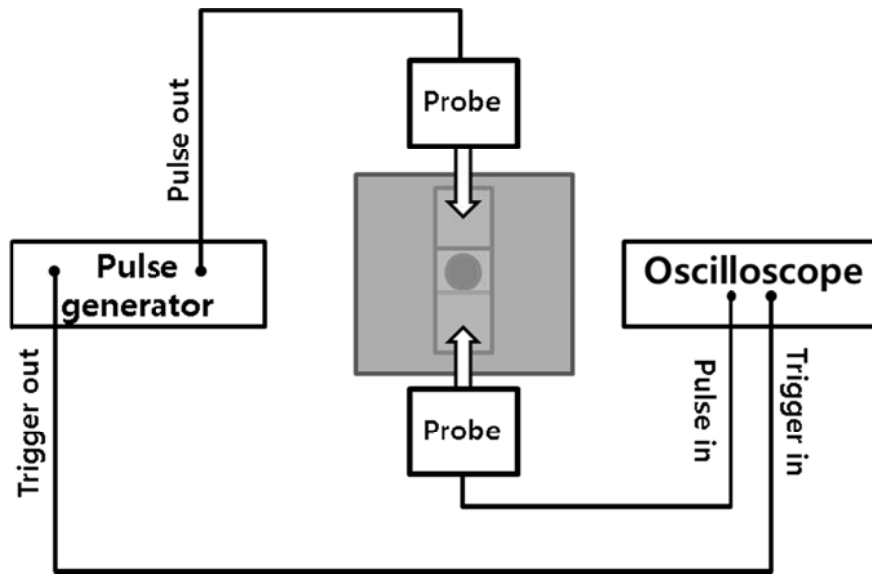
Fig. A.13 Schematic illustration of our electrical measurement setup .
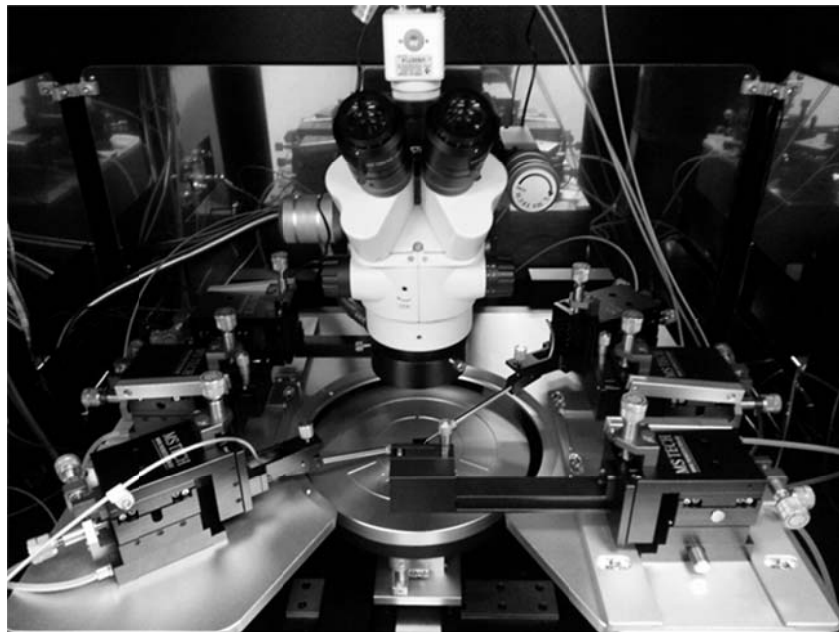
Fig. A.14 Picture of our probe station.
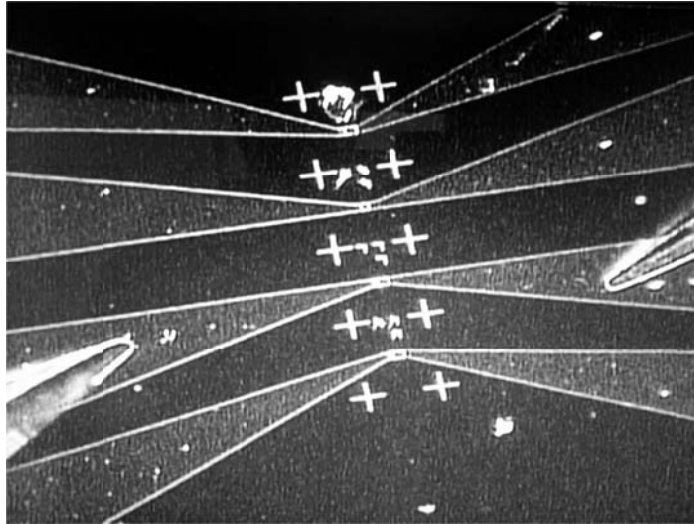
Fig. A.15 Optical microscope image of the patterned sample. Two probes are contacted on the electrodes of the third sample.
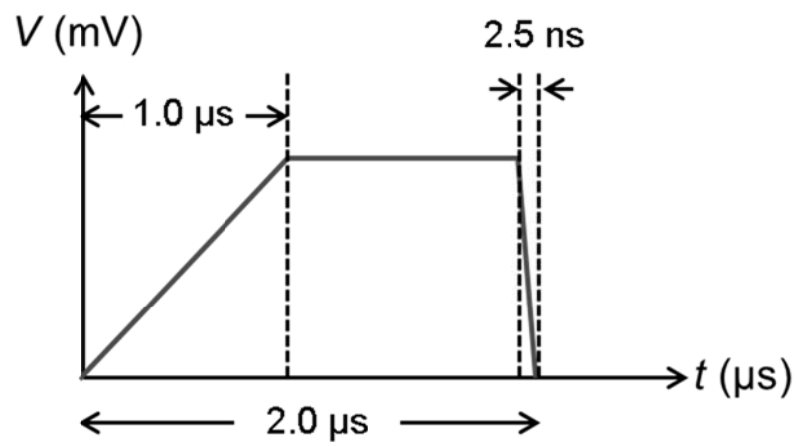
Fig. A.16 The duration time, raising edge, and end edge of the applied current pulse.

References

[1] A. Hubert and R. Schafer, Magnetic domains Springer, Berlin, 1998.

[2] T. Shinjo, T. Okuno, R. Hassdorf, K. Shigeto, and T. Ono, Magnetic Vortex Core Observation in Circular Dots of Permalloy, Science, 289 930 (2000).

[3] A. Wachowiak, J. Wiebe, M. Bode, O. Pietzsch, M. Morgenstern, and R. Wiesendanger, Direct Observation of Internal Spin Structure of Magnetic Vortex Cores, Science, 298 577 (2002).

[4] S.-K. Kim, K.-S. Lee, B.-W. Kang, K.-J. Lee, and J.B. Kortright, Vortex-antivortex assisted magnetization dynamics in a semi-continuous thin-film model system studied by micromagnetic simulations, Applied Physics Letters, 86 052504-052503 (2005).

[5] K.L. Metlov and K.Y. Guslienko, Stability of magnetic vortex in soft magnetic nano-sized circular cylinder, Journal of Magnetism and Magnetic Materials, 242–245, Part 2 1015-1017 (2002).

[6] R.P. Cowburn, D.K. Koltsov, A.O. Adeyeye, M.E. Welland, and D.M. Tricker, Single-Domain Circular Nanomagnets, Physical Review Letters, 83 1042-1045 (1999).

[7] K.Y. Guslienko, B.A. Ivanov, V. Novosad, Y. Otani, H. Shima, and K. Fukamichi, Eigenfrequencies of vortex state excitations in magnetic submicron-size disks, Journal of Applied Physics, 91 8037 (2002).

[8] J.P. Park, P. Eames, D.M. Engebretson, J. Berezovsky, and P.A. Crowell, Imaging of spin dynamics in closure domain and vortex structures, Physical Review B, 67 020403 (2003).

[9] V. Novosad, F.Y. Fradin, P.E. Roy, K.S. Buchanan, K.Y. Guslienko, and S.D. Bader, Magnetic vortex resonance in patterned ferromagnetic dots, Physical Review B, 72 024455 (2005).

[10] K.-S. Lee and S.-K. Kim, Two circular-rotational eigenmodes and their giant resonance asymmetry in vortex gyrotropic motions in soft magnetic nanodots, Physical Review B, 78   (2008).

[11] S.-K. Kim, K.-S. Lee, Y.-S. Yu, and Y.-S. Choi, Reliable low-power control of ultrafast vortex-core switching with the selectivity in an array of vortex states by in-plane circular-rotational magnetic fields and spin-polarized currents, Applied Physics Letters, 92 022509 (2008).

[12] J.C. Slonczewski, Current-driven excitation of magnetic multilayers, Journal of Magnetism and Magnetic Materials, 159 L1-L7 (1996).

[13] L. Berger, Emission of spin waves by a magnetic multilayer traversed by a current, Physical Review B, 54 9353-9358 (1996).

[14] M. Tsoi, A.G.M. Jansen, J. Bass, W.C. Chiang, M. Seck, V. Tsoi, and P. Wyder, Excitation of a Magnetic Multilayer by an Electric Current, Physical Review Letters, 80 4281-4284 (1998).

[15] S.I. Kiselev, J.C. Sankey, I.N. Krivorotov, N.C. Emley, R.J. Schoelkopf, R.A. Buhrman, and D.C. Ralph, Microwave oscillations of a nanomagnet driven by a spin-polarized current, Nature, 425 380-383 (2003).

[16] I. Firastrau, D. Gusakova, D. Houssameddine, U. Ebels, M.C. Cyrille, B. Delaet, B. Dieny, O. Redon, J.C. Toussaint, and L.D. Buda-Prejbeanu, Modeling of the perpendicular polarizer-planar free layer spin torque oscillator: Micromagnetic simulations, Physical Review B, 78 024437 (2008).

[17] V.S. Pribiag, I.N. Krivorotov, G.D. Fuchs, P.M. Braganca, O. Ozatay, J.C. Sankey, D.C. Ralph, and R.A. Buhrman, Magnetic vortex oscillator driven by d.c. spin-polarized current, Nat Phys, 3 498-503 (2007).

[18] Q. Mistral, M. van Kampen, G. Hrkac, J.-V. Kim, T. Devolder, P. Crozat, C. Chappert, L. Lagae, and T. Schrefl, Current-Driven Vortex Oscillations in Metallic Nanocontacts, Physical Review Letters, 100 (2008).

[19] S. Kasai, Y. Nakatani, K. Kobayashi, H. Kohno, and T. Ono, Current-Driven Resonant Excitation of Magnetic Vortices, Physical Review Letters, 97 107204 (2006).

[20] B.A. Ivanov and C.E. Zaspel, Excitation of Spin Dynamics by Spin-Polarized Current in Vortex State Magnetic Disks, Physical Review Letters, 99 247208 (2007).

[21] M. Bolte, G. Meier, B. Krüger, A. Drews, R. Eiselt, L. Bocklage, S. Bohlens, T. Tyliszczak, A. Vansteenkiste, B. Van Waeyenberge, K.W. Chou, A. Puzic, and H. Stoll, Time-Resolved X-Ray Microscopy of Spin-Torque-Induced Magnetic Vortex Gyration, Physical Review Letters, 100 176601 (2008).

[22] K. Yamada, S. Kasai, Y. Nakatani, K. Kobayashi, H. Kohno, A. Thiaville, and T. Ono, Electrical switching of the vortex core in a magnetic disk, Nature materials, 6 269-263 (2007).

[23] J.-G. Caputo, Y. Gaididei, F.G. Mertens, and D.D. Sheka, Vortex Polarity Switching by a Spin-Polarized Current, Physical Review Letters, 98 056604 (2007).

[24] S.-K. Kim, Y.-S. Choi, K.-S. Lee, K.Y. Guslienko, and D.-E. Jeong, Electric-current-driven vortex-core reversal in soft magnetic nanodots, Applied Physics Letters, 91 082506 (2007).

[25] Y. Liu, H. He, and Z. Zhang, Spin-torque-driven vortex dynamics in a spin-valve pillar with a perpendicular polarizer, Applied Physics Letters, 91 242501-242503 (2007).

[26] D.D. Sheka, Y. Gaididei, and F.G. Mertens, Current induced switching of vortex polarity in magnetic nanodisks, Applied Physics Letters, 91 082509-082503 (2007).

[27] A. Tonomura, T. Matsuda, J. Endo, T. Arii, and K. Mihama, Direct Observation of Fine Structure of Magnetic Domain Walls by Electron Holography, Physical Review Letters, 44 1430-1433 (1980).

[28] A. Fert, P. Grünberg, A. Barthélémy, F. Petroff, and W. Zinn, Layered magnetic structures: interlayer exchange coupling and giant magnetoresistance, Journal of Magnetism and Magnetic Materials, 140–144, Part 1 1-8 (1995).

[29] P.M. Levy, Current understanding and open questions on giant magnetoresistance, Journal of Magnetism and Magnetic Materials, 140–144, Part 1 485-487 (1995).

[30] E.B. Myers, Current-Induced Switching of Domains in Magnetic Multilayer Devices, Science, 285 867-870 (1999).

[31] J.A. Katine, F.J. Albert, R.A. Buhrman, E.B. Myers, and D.C. Ralph, Current-Driven Magnetization Reversal and Spin-Wave Excitations in Co /Cu /Co Pillars, Physical Review Letters, 84 3149-3152 (2000).

[32] D.C. Ralph and M.D. Stiles, Spin transfer torques, Journal of Magnetism and Magnetic Materials, 320 1190-1216 (2008).

[33] J.Z. Sun and D.C. Ralph, Magnetoresistance and spin-transfer torque in magnetic tunnel junctions, Journal of Magnetism and Magnetic Materials, 320 1227-1237 (2008).

[34] J. Xiao, A. Zangwill, and M.D. Stiles, Boltzmann test of Slonczewski's theory of spin-transfer torque, Physical Review B, 70 172405 (2004).

[35] L.D. Landau and E.M. Lifshitz, On the theory of the dispersion of magnetic permeability in ferromagnetic bodies, Phys. Z. Sowjetunion, 8 153 (1935).

[36] K.-S. Lee, Dynamics of magnetic vortex excitations in soft magnetic nanoelements, Ph. D thesis, Seoul National University, South Korea, (2010).

[37] S. Zhang and Z. Li, Roles of Nonequilibrium Conduction Electrons on the Magnetization Dynamics of Ferromagnets, Physical Review Letters, 93 (2004).

[38] A.A. Thiele, Steady-State Motion of Magnetic Domains, Physical Review Letters, 30 230-233 (1973).

[39] B. Van Waeyenberge, A. Puzic, H. Stoll, K.W. Chou, T. Tyliszczak, R. Hertel, M. Fahnle, H. Bruckl, K. Rott, G. Reiss, I. Neudecker, D. Weiss, C.H. Back, and G. Schutz, Magnetic vortex core reversal by excitation with short bursts of an alternating field, Nature, 444 461-464 (2006).

[40] T. Ishida, T. Kimura, and Y. Otani, Current-induced vortex displacement and annihilation in a single permalloy disk, Physical Review B, 74 014424 (2006).

126

[41] J. Shibata, Y. Nakatani, G. Tatara, H. Kohno, and Y. Otani, Magnetic vortex dynamics induced by spin-transfer torque, Journal of Magnetism and Magnetic Materials, 310 2041-2042 (2007).

[42] M. R. Scheinfein, LLG MICROMAGNETIC SIMULATOR™.

[43] K.-S. Lee, S. Choi, and S.-K. Kim, Radiation of spin waves from magnetic vortex cores by their dynamic motion and annihilation processes, Applied Physics Letters, 87 192502-192503 (2005).

[44] S. Choi, K.-S. Lee, K.Y. Guslienko, and S.-K. Kim, Strong Radiation of Spin Waves by Core Reversal of a Magnetic Vortex and Their Wave Behaviors in Magnetic Nanowire Waveguides, Physical Review Letters, 98 087205 (2007).

[45] R. Hertel, S. Gliga, M. Fähnle, and C.M. Schneider, Ultrafast Nanomagnetic Toggle Switching of Vortex Cores, Physical Review Letters, 98 117201 (2007).

[46] K.Y. Guslienko, K.-S. Lee, and S.-K. Kim, Dynamic Origin of Vortex Core Switching in Soft Magnetic Nanodots, Physical Review Letters, 100 027203 (2008).

[47] K.-S. Lee, Y.-S. Yu, Y.-S. Choi, D.-E. Jeong, and S.-K. Kim, Oppositely rotating eigenmodes of spin-polarized current-driven vortex gyrotropic motions in elliptical nanodots, Applied Physics Letters, 92 192513 (2008).

[48] K.Y. Guslienko, Low-frequency vortex dynamic susceptibility and relaxation in mesoscopic ferromagnetic dots, Applied Physics Letters, 89 022510-022513 (2006).

[49] P.O. Jubert and R. Allenspach, Analytical approach to the single-domain-to-vortex transition in small magnetic disks, Physical Review B, 70 144402 (2004).

[50] S. Bohlens, B. Kruger, A. Drews, M. Bolte, G. Meier, and D. Pfannkuche, Current controlled random-access memory based on magnetic vortex handedness, Applied Physics Letters, 93 142508-142503 (2008).

[51] B.C. Choi, J. Rudge, E. Girgis, J. Kolthammer, Y.K. Hong, and A. Lyle, Spin-current pulse induced switching of vortex chirality in permalloy/Cu/Co nanopillars, Applied Physics Letters, 91 022501-022503 (2007).

[52] T. Yang, M. Hara, A. Hirohata, T. Kimura, and Y. Otani, Magnetic characterization and switching of Co nanorings in current-perpendicular-to-plane configuration, Applied Physics Letters, 90 022504-022503 (2007).

[53] Y.-S. Choi, S.-K. Kim, K.-S. Lee, and Y.-S. Yu, Understanding eigenfrequency shifts observed in vortex gyrotropic motions in a magnetic nanodot driven by spin-polarized out-of-plane dc current, Applied Physics Letters, 93 182508 (2008).

[54]   http://math.nist.gov/oommf..

[55] Y.-S. Choi, K.-S. Lee, and S.-K. Kim, Quantitative understanding of magnetic vortex oscillations driven by spin-polarized out-of-plane dc

current: Analytical and micromagnetic numerical study, Physical Review B, 79 184424 (2009).

[56] Y.-S. Yu, Gaussian-Pulse-Induced Magnetic Vortex Dynamics in Ferromagnetic Nanostructures, Ph. D thesis, Seoul National University, South Korea, (2012).

Publications

(1) H. Jung, **Y.-S. Choi**, K.-S. Lee, D.-S. Han, Y.-S. Yu, M.-Y. Im, P. Fischer, and S.-K. Kim, ACS Nano 6, 3712–3717 (2012).

"Logic Operations Based on Magnetic-Vortex-State Networks"

(2) H. Jung, K.-S. Lee, D.-E. Jeong, **Y.-S. Choi**, Y.-S. Yu, D.-S. Han, A. Vogel, L. Bocklage, G. Meier, M.-Y. Im, P. Fischer and S.-K. Kim, Scientific Reports (Nature Publishing Group) 1, 59; DOI:10.1038/srep00059 (2011).

"Tunable negligible-loss energy transfer between dipolar-coupled magnetic disks by stimulated vortex gyration"

(3) Y.-S. Yu, K.-S. Lee, H. Jung, **Y.-S. Choi**, M.-W. Yoo, D.-S. Han, M.-Y. Im, P. Fischer, and S.-K. Kim, Phys. Rev. B. 83, 174429 (2011).

"Polarization-selective vortex-core switching by tailored orthogonal Gaussian-pulse currents"

⇒ Selected for the Virtual Journal of Nanoscale Science & Technology [May 30, 2011, Volume 23, Issue 21]

(4)   K.-S. Lee, M.-W. Yoo, **Y.-S. Choi**, and S.-K. Kim, Phys. Rev. Lett. 106, 147201 (2011)

"Edge-soliton-mediated vortex-core reversal dynamics"

⇒ Selected for the Virtual Journal of Nanoscale Science & Technology

[Apr. 18, 2011, Volume 23, Issue 15]

(5)   **Y.-S. Choi**, M.-W. Yoo, K.-S. Lee, Y.-S. Yu, H. Jung, and S.-K. Kim, Appl. Phys. Lett. **96**, 072507 (2010).

"Out-of-plane current controlled switching of the fourfold degenerate state of a magnetic vortex in soft magnetic nanodots"

(6)   **Y.-S. Choi**, J.-Y. Lee, M.-W. Yoo, K.-S. Lee, K. Yu. Guslienko, and S.-K. Kim, Phys. Rev. B. 80, 012402 (2009)

"Critical nucleation size of vortex core for domain wall transformation in soft magnetic thin-film nanostrips"

(7)   **Y.-S. Choi**, K.-S. Lee, and S.-K. Kim, Phys. Rev. B. 79, 184424 (2009)

"Quantitative understanding of magnetic vortex oscillations driven by spin-polarized out-of-plane dc current: Analytical and micromagnetic numerical study"

(8) S.-K. Kim, K.-S. Lee, **<u>Y.-S. Choi</u>**, and Y.-S. Yu, IEEE Trans. Mag. 44 (2008).

*Proceeding of the IEEE International Magnetic Conference 2008 (Intermag 2008)

"Low-Power Selective Control of Ultrafast Vortex-Core Switching by Circularly Rotating Magnetic Fields: Circular-Rotational Eigenmodes"

(9) K.-S. Lee, S.-K. Kim, Y.-S. Yu, **<u>Y.-S. Choi</u>**, K. Yu. Guslienko, H. Jung, and P. Fischer, Phys. Rev. Lett. **101**, 267206 (2008).

"Universal criterion and phase diagram for switching a magnetic vortex core in soft magnetic nanodots"

⇒ Selected for the Virtual Journal of Nanoscale Science & Technology [Jan. 12, 2009, Volume 19, Issue 2]

⇒ Selected for the Virtual Journal of Ultrafast Science [Jan, 2009, Volume 8, Issue 1]

(10) **<u>Y.-S. Choi</u>**, S.-K. Kim, K.-S. Lee, and Y.-S. Yu, Appl. Phys. Lett. **93**, 182508 (2008).

"Understanding eigenfrequency shifts observed in vortex gyrotropic motions in a magnetic nanodot driven by spin-polarized out-of-plane dc current"

⇒ Selected for the Virtual Journal of Nanoscale Science & Technology [Nov. 24, 2008, Volume 18, Issue 21]

132

(11) S.-K. Kim, J.-Y. Lee, **<u>Y.-S. Choi</u>**, K. Yu. Guslienko, and K.-S. Lee, Appl. Phys. Lett. 93, 052503 (2008)

"Underlying Mechanism of Domain-Wall Motions in Soft Magnetic Thin-Film Nanostripes Beyond the Velocity-Breakdown Regime"

⇒ Selected for the Virtual Journal of Nanoscale Science & Technology

[Aug. 18, 2008, Volume 18, Issue 7]

(12) S.-K. Kim, S. Choi, K.-S. Lee, D.-S. Han, D.-E. Jung, and **<u>Y.-S. Choi</u>**, Appl. Phys. Lett. 92, 212501 (2008)

"Negative refraction of dipole-exchange spin waves through a magnetic twin interface in restricted geometry"

(13) K.-S. Lee, Y.-S. Yu, **<u>Y.-S. Choi</u>**, D.-E. Jeong, and S.-K. Kim, Appl. Phys. Lett. **92**, 192513 (2008).

"Oppositely rotating eigenmodes of spin-polarized current-driven vortex gyrotropic motions in elliptical nanodots"

(14) S.-K. Kim, K.-S. Lee, Y.-S. Yu, and **<u>Y.-S. Choi</u>**, Appl. Phys. Lett. 92, 022509 (2008).

"Reliable low-power control of ultrafast vortex-core switching with the selectivity in arrays of vortex states by in-plane circular-rotational magneticfields and spin-polarized currents"

⇒ Selected as the cover of the 14 Jan. 2008 issue

(15)   S.-K. Kim, **Y.-S. Choi**, K.-S. Lee, K. Y. Guslienko, and D.-E. Jeong, Appl.

Phys. Lett. 91, 082506 (2007)

"Electric-current-driven vortex-core reversal in soft magnetic nanodots"

⇒ Selected for the Virtual Journal of Nanoscale Science & Technology

[Sep. 3, 2007, Volume 16, Issue 10]

International Conference Presentations

(1) [2011] 56th Annual Conference on Magnetism & Magnetic Materials (MMM 2011), Arizona, USA, Oct. 30- Nov. 3, 2011.

Y.-S. Yu, K.-S. Lee, H. Jung, **Y.-S. Choi**, J.-Y. Lee, M.-W. Yoo, D.-S. Han, M.-Y. Im, P. Fischer, and S.-K. Kim

"Reliable energy-efficient information recording by tailored orthogonal pulse currents in vortex-core cross-point architecture"

(2) [2011] 56th Annual Conference on Magnetism & Magnetic Materials (MMM 2011), Arizona, USA, Oct. 30- Nov. 3, 2011.

H. Jung, K.-S. Lee, D.-E. Jeong, **Y.-S. Choi**, Y.-S. Yu, D-.S. Han, A. Vogel, L. Bocklage, G. Meier, M.-Y. Im, P. Fischer, S.-K. Kim

"Tunable negligible-loss energy transfer between dipolar-coupled magnetic disks by stimulated vortex gyration"

(3) [2010] International Conference of AUMS (ICAUMS 2010), Jeju, Korea, Dec. 5 - 8, 2010.

Y.-S. Choi, M.-W. Yoo, K.-S. Lee, Y.-S. Yu, H. Jung, and S.-K. Kim

"Switching of vortex fourfold ground states by out-of-plane pulse currents"

(4)   [2010] International Conference of AUMS (ICAUMS 2010), Jeju, Korea, Dec. 5 - 8, 2010.

Y.-S. Yu, K.-S. Lee, H. Jung, **Y.-S. Choi**, J.-Y. Lee, M.-W. Yoo, D.-S. Han, M.-Y. Im, P. Fischer and S.-K. Kim

"Unipolar Gaussian-pulse current driven vortex core switching in cross-point architecture"

(5)   [2010] 55th Annual Conference on Magnetism & Magnetic Materials (MMM 2010), Atlanta, USA, Nov. 14 - 18, 2010.

Y.-S. Yu, K.-S. Lee, H. Jung, **Y.-S. Choi**, J.-Y. Lee, M.-W. Yoo, D.-S. Han, M.-Y. Im, P. Fischer, and S.-K. Kim

"Unipolar Gaussian-Pulse Current Driven Vortex Core Switching in Cross-Point Architecture"

(6)   [2010] 55th Annual Conference on Magnetism & Magnetic Materials (MMM 2010), Atlanta, USA, Nov. 14 - 18, 2010.

K.-S. Lee, M.-W. Yoo, **Y.-S. Choi**, D.-E. Jeong and S.-K. Kim

"Exploring underlying physics of edge-soliton mediated vortex-core switching dynamics"

(7)   [2010] IEEE 7th International Symposium on Metallic Multilayers (MML 2010), California, USA, Sep. 19 - 24, 2010.

Y.-S. Yu, K.-S. Lee, H. Jung, **Y.-S. Choi**, J.-Y. Lee, M.-W. Yoo, D.-S. Han, M.-Y. Im, P. Fischer, and S.-K. Kim

"Lower-Power Consumption And Nonvolatile Vortex-Core Random Acess Memory"

(8)   [2009] IEEE International Magnetics Conference (INTERMAG 2009), Sacramento, California, USA, May 4 ~ 8, 2009.

Y.-S. Choi, K.-S. Lee, and S.-K. Kim

"Magnetic vortex oscillators driven by spin-polarized out-of-plane dc current"

(9)   [2009] IEEE International Magnetics Conference (INTERMAG 2009), Sacramento, California, USA, May 4 ~ 8, 2009.

K.-S. Lee, S.-K. Kim, Y.-S. Yu, **Y.-S. Choi**, H. Jung, K. Yu. Guslienko, and P. Fischer

"Phase diagrams for vortex-core switching threshold field and switching time"

(10)   [2009] Materials Research Society (MRS) Spring Meeting, San Francisco, USA, April 13 ~ 17, 2009.

S.-K. Kim, K.-S. Lee, Y.-S. Yu, **Y.-S. Choi**, K. Yu Guslienko, H. Jeong, and D.-E. Jeong

"Magnetic vortex dynamics: from fundamentals to applications"

137

(11)   [2008] Asian Magnetics Conference 2008 (AMC 2008), Busan, South
        Korea, Dec. 10 - 13, 2008.

        Y.-S. Choi, K.-S. Lee, H. Jung, and S.-K. Kim

        "Out-of-plane DC Current Driven Vortex Excitations in Soft Magnetic
        Nanodots:Vortex Gyrotropic Motion and Vortex-core Reversal Behaviors"

(12)   [2008] Asian Magnetics Conference 2008 (AMC 2008), Busan, South
        Korea, Dec. 10 - 13, 2008.

        Y.-S. Yu, K.-S. Lee, **Y.-S. Choi**, D.-E. Jeong, and S.-K. Kim

        "Resonant and Non-resonant Rotating Eigenmodes of Current-driven Vortex
        Gyrotropic Motions in Soft Magnetic Elliptical Nanodots"

(13)   [2008] Asian Magnetics Conference 2008 (AMC 2008), Busan, South
        Korea, Dec. 10 - 13, 2008.

        K.-S. Lee, S.-K. Kim, Y.-S. Yu, **Y.-S. Choi**, H. Jung, K. Yu Guslienko, and
        P. Fischer

        "Critical Velocity of Vortex Core Motions as the Universal Criterion for
        Core Magnetization Reversals in Soft Magnetic Nanodots"

(14)   [2008] Asian Magnetics Conference 2008 (AMC 2008), Busan, South
        Korea, Dec. 10 - 13, 2008.

        S.-K. Kim, K.-S. Lee, Y.-S. Yu, **Y.-S. Choi**, H. Jung, and D.-E. Jeong

        "Vortex Random Access Memory (VRAM) as New MRAM Scheme"

138

(15)   [2008] Asian Magnetics Conference 2008 (AMC 2008), Busan, South

Korea, Dec. 10 - 13, 2008.

S.-K. Kim, **Y.-S. Choi**, J.-Y. Lee, K. Yu Guslienko, K.-S. Lee, and M.-W.

Yoo

"Universal Criterion for Formation of Stable Vortex or Antivortex in

Domain Wall Motions in Magnetic Thin-film Nanostripes: Two

Dimensional Soliton Model"

(16)   [2008] 53rd Annual Conference on Magnetism and Magnetic Materials

(MMM 2008), Texas, USA, Nov. 10 - 14, 2008.

S.-K. Kim, **Y.-S. Choi**, and M.-W. Yoo

"Critical vortex core size required for nucleation of stable vortex or

antivortex during domain wall motion in magneticthin-film nanostripes"

(17)   [2008] 53rd Annual Conference on Magnetism and Magnetic Materials

(MMM 2008), Texas, USA, Nov. 10 - 14, 2008.

S.-K. Kim, K.-S. Lee, Y.-S. Yu, **Y.-S. Choi**, H. Jung and D.-E. Jeong

"Vortex random access memory (VRAM) as new MRAM scheme"

(18)   [2008] Gordon Research Conferences, Aussois, France, Aug. 31 – Sep. 5,

2008.

S.-K. Kim, K.-S. Lee, Y.-S. Yu, **Y.-S. Choi**, K. Yu Guslienko, D.-E. Jung,

H. Jung

"Novel dynamic properties of magnetic vortex in soft magnetic nanodots"

(19) [2008] Joint European Magnetic Symposia (JEMS 2008), Dublin, Ireland,

Sep. 14 – 19, 2008.

K.-S. Lee, S.-K. Kim, Y.-S. Yu, **Y.-S. Choi**, and D.-E. Jeong

"Magnetic field- and spin-polarized current- driven gyrotropic motion of a

magnetic vortex in magnetic nanoelements and the oppositely rotating

eigenmodes"

(20) [2008] IEEE Internatinoal Magnetic Conference 2008 (Intermag 2008)

K.-S. Lee, S.-K. Kim, D.-E. Jung, Y.-S. Yu, and **Y.-S. Choi**

"Elementary Circular Eigenmodes of the Magnetic Vortex Gyrotropic

Motion: Application to the Reliable Low-power Control of Ultrafast Vortex-

core Switching"

(21) [2007] 52nd Magnetism and Magnetic Materials Conference, Tampa,

Florida, USA, Nov. 5-9, 2007.

K.-S. Lee, D.-E. Jeong, **Y.-S. Choi**, Y.-S. Yu, K. Guslienko, and S.-K. Kim

"Elementary circular eigenmotions of a magnetic vortex core in linear

regime"

(22) [2007] 52nd Magnetism and Magnetic Materials Conference, Tampa,

Florida, USA, Nov. 5-9, 2007.

S.-K. Kim, K.-S. Lee, J.-Y. Lee, K. Y. Guslienko, Y.-S. Yu, **Y.-S. Choi**, D.-

E. Jeong

"Vortex Dynamics in Patterned Ferromagnetic Films: Gyromotion,

Reversal, and Domain-Wall Transformation"

140

국문 초록

수 마이크로 이하로 패턴된 연자성 박막에서는 박막의 지름과 두께에 따라 스핀 소용돌이라는 구조가 안정한 상태를 가질 수 있게 된다. 스핀 소용돌이는 박막 면 중심의 수십 나노 크기의 영역에서 박막 면과 수직한 스핀 배열 구조를 갖는 스핀 소용돌이 핵과, 스핀 소용돌이 핵 주변에서 스핀들이 꼬리에 꼬리를 무는 형상을 보이며 박막 면에 평행하게 배열되어 있는 키랄리티(chirality)로 구성된다. 이 때, 스핀 소용돌이 핵은 "위" 또는 "아래" 방향을 가질 수 있고, 키랄리티의 스핀 배열은 "시계방향" 또는 "반시계방향" 을 가질 수 있다. 또한, 스핀 소용돌이 구조에 외부 자기장(또는 전류)을 인가하면 스핀 소용돌이 핵의 회전 운동을 발생시킬 수 있다. 이러한 특성으로 인해 스핀 소용돌이 구조는 나노 진동자 또는 정보 저장 소자로서의 응용성을 인정받아 많은 사람들의 관심 속에 연구가 진행되어 왔다. 본 학위 논문에서는 전류 인가 시에 발생하는 스핀 전달 토크를 이용하여 스핀 소용돌이 핵의 회전 운동 및 자화반전 현상을 이론 및 전산모사를 통해 연구 분석하였다.

스핀 소용돌이 구조에서 박막 면에 평행한 방향으로 사인 펄스 (sine pulse)의 전류를 인가할 때 스핀 소용돌이 핵의 자화반전이

141

발생하는 것을 발견하였고, 자화반전의 메커니즘(mechanism)을 전산모사를 통해 규명하였다. 또한, 스핀 소용돌이 핵의 자화반전이 일어날 때 스핀파(spin-wave)가 발생하는 것을 관측하였다.

한편, 박막 면에 수직한 방향으로 스핀 편향 전류(spin polarized current)를 인가할 때 스핀 소용돌이 핵의 회전 운동이 발생하는 것을 관측하였으며, 전류 인가 시 발생하는 외스테드 자기장(Oersted field)과 스핀의 상호작용에 의해 스핀 소용돌이 핵의 회전 진동수가 변화하는 것을 관측하였다. 또한, 스핀 편향 전류에 의해 발생하는 스핀 소용돌이 핵의 회전운동을 이론적으로 계산하여 스핀 소용돌이 핵의 회전운동을 위한 한계 전류 값을 예측하였으며, 스핀 소용돌이 구조의 지름 및 두께에 따른 한계 전류 값 및 회전 진동수를 이론적으로 계산하였다.

마지막으로, 스핀 편향 전류의 세기에 따라 스핀 소용돌이의 동적 거동이 변화하는 것을 관측하였으며, 이를 바탕으로 스핀 소용돌이 핵 또는 키랄리티의 자화반전을 각각 독립적으로 제어할 수 있는 방법을 제시하였다. 또한, 이를 이용하여 스핀 소용돌이 구조에서 스핀 편향 전류를 이용한 멀티 비트 메모리 소자의 가능성을 제시하였다.

감사의 글

관악산의 아름다운 벚꽃을 바라보며 공학도의 꿈을 키워 온지도 벌써 10 여년의 세월이 흘렀습니다. 이제 다시 새로운 인생의 시작점에 서서 한 발 내디딜 시간입니다. 아직 제 자신이 나아가야 할 길에 대한 정확한 답을 찾지 못해 두려움이 앞서지만 박사 과정을 하며 배운 경험을 토대로 이를 헤쳐나갈 수 있을 것이라 생각합니다. 지금까지 저를 옆에서 지켜봐 주시고 격려해주신 많은 분들께 이 글을 통해 감사의 마음을 전하고자 합니다.

연구가 무엇인지를 알게 해주시고 학문에 대한 열정과 창의적인 사고로써 항상 저를 일깨워 주신 저의 지도 교수님, 김상국 교수님께 감사를 드립니다. 그리고 학위 논문을 지도해주신 오규환 교수님, 황철성 교수님, 홍성현 교수님, 그리고 민병철 박사님께도 감사를 드립니다.

저와 수 년간 대학원 생활을 같이하며 동고동락 해온 연구실 동료들에게 감사의 마음을 전합니다. 제가 지금의 자리에 오기까지 멘토의 역할을 해주신 기석이 형 감사드립니다. 때로는 친구로, 때로는 듬직한 형님으로 함께 했던 대은이 형 감사드립니다. 항상 하나님의 말씀 아래서 많은 조언을 해주신 재완이 형 감사드립니다. 함께

143

술마시며 웃고 떠들던 시간이 엊그제 같은데 이제는 모두 자신의 미래를 위해 걸어가고 있는 형제 같았던 준영이, 작은 윤석이, 종우에게도 감사의 말을 전하고 싶습니다. 연구실에서 친구이자 선배로서 많은 시간을 함께 했던 영상이 에게도 감사의 말을 전하고 싶습니다. 실험 및 졸업으로 함께 고민했던 현성이, 아이 같았던 신입생 시절을 뒤로 하고 이제는 연구실의 지배자가 되고자 하는 동수에게도 감사의 말을 전하고 싶습니다. 저의 뒤를 이어서 랩실의 방장으로 랩실을 이끌어 나가는 명우, 연구실의 칙칙한 분위기를 바꿔준 하연이, 지혜에게도 감사의 말을 전하고 싶습니다. 나이 차이는 많이 나지만 항상 잘 따르고 웃는 얼굴로 궂은 일도 마다 않던 보성이와 준회, 연구보다는 다른 일로 더 많은 이야기를 나눈 것 같은 영준이와 민관이, 랩실의 막내 부산 사나이 한별이 에게도 감사의 말을 전하고 싶습니다.

고등학교 시절부터 대학원을 졸업하는 이 시간까지도 항상 함께 하고 있는 한성 과학고 친구들과, 제 인생의 더없이 좋은 추억이 된 서울대 합창단 친구들에게도 감사드립니다. 지금까지 변함없이 우정을 간직하며 살아가고 있는 우석이, 우선이, 영훈이, 태휘, 형국이, 진우 에게도 감사의 말을 전합니다. 죽는 날까지 자주 모이며 기쁨과 슬픔을 함께 나눌 수 있기를 바랍니다.

지금의 제가 있기까지 저를 키워주시고, 돌봐주시고, 바른 길로 이끌어주신 저의 부모님, 이제는 두 번째 부모님이 된, 항상 저를

144

아들처럼 아껴주시는 장인 어른, 장모님께도 감사의 말을 전하고 싶습니다. 저의 하나뿐인 동생 현정이 에게도 감사의 말을 전하고 싶습니다.

석사 시절 결혼해서 힘든 대학원 생활을 항상 함께 견뎌왔던 사랑하는 아내 주선이에게 누구보다 감사하다는 말을 전하고 싶습니다. 대학원 생활 동안의 어려움이 먼 훗날 즐거운 추억이 될 것이라 믿어 의심치 않습니다. 앞으로 대학원 생활 동안 못했던 많은 것들을 하나하나 해보면서 행복하게 살아갑시다.

마지막으로, 지금의 제가 있기까지 언제나 함께 해주신 하나님 아버지께 이 논문을 바칩니다.

<div align="right">

겨울의 끝자락에 선 관악에서

최 윤 석

</div>

<div align="center">

145

</div>